Article

Forward and Reverse Waves: Modeling Distortion Products in the Intracochlear Fluid Pressure

Thomas Bowling[1] and Julien Meaud[1,2,*]

[1]G.W.W. School of Mechanical Engineering and [2]Petit Institute for Bioengineering and Bioscience, Georgia Institute of Technology, Atlanta, Georgia

ABSTRACT   Distortion product otoacoustic emissions are sounds that are emitted by the cochlea due to the nonlinearity of the outer hair cells. These emissions play an important role both in clinical settings and research laboratories. However, how distortion products propagate from their generation location to the middle ear remains unclear; whether distortion products propagate as a slow reverse traveling wave, or as a fast compression wave, through the cochlear fluid has been debated. In this article, we evaluate the contributions of the slow reverse wave and fast compression wave to the propagation of intracochlear distortion products using a physiologically based nonlinear model of the gerbil cochlea. This model includes a 3D two-duct model of the intracochlear fluid and a realistic model of outer hair cell biophysics. Simulations of the distortion products in the cochlear fluid pressure in response to a two-tone stimulus are compared with published in vivo experimental results. Whereas experiments have characterized distortion products at a limited number of locations, this model provides a complete description of the fluid pressure at all locations in the cochlear ducts. As in experiments, the spatial variations of the distortion products in the fluid pressure have some similarities with what is observed in response to a pure tone. Analysis of the fluid pressure demonstrates that although a fast wave component is generated, the slow wave component dominates the response. Decomposition of the model simulations into forward and reverse wave components shows that a slow forward propagating wave is generated due to the reflection of the slow reverse wave at the stapes. Wave interference between the reverse and forward components sometimes complicates the analysis of distortion products propagation using measurements at a few locations.

INTRODUCTION

The cochlea is a fluid-filled biological sensory system with high frequency selectivity, high sensitivity, and a wide dynamic range that spans several orders of magnitude (1). The nonlinear active feedback mechanism behind these characteristics originates from the outer hair cells (OHCs) and is commonly called the "cochlear amplifier" (2). Because of the active OHC feedback, the healthy cochlea can generate sounds, called "otoacoustic emissions" (3). Because otoacoustic emissions can be easily measured by placing a probe in the ear canal, they are commonly used both clinically and in research to study the functional status and biophysics of the ear (e.g., (4–6)). The focus of this article is on a specific type of otoacoustic emissions called "distortion product otoacoustic emissions" (DPOAEs); DPOAEs are generated by OHCs due to the nonlinear interaction of two stimulus tones (of frequencies f_1 and f_2, where $f_2 > f_1$) (7). Intracochlear measurements of the basilar

membrane (BM) velocity (8–10) or fluid pressure (11) in response to a two-tone stimulus have confirmed that distortion products (DPs) are generated in the cochlea. It is generally agreed that DPOAEs are generated by the OHCs (8) due to the nonlinearity of the mechanoelectrical transduction (MET) channel (12). In any nonlinear system, DPs occur at linear combinations of the two stimulus tones; due to the specific form of cochlear nonlinearity, the low-side cubic DP of frequency, $f_{DP} = 2f_1 - f_2$, tends to have the highest amplitude and is the most commonly studied DP (10).

In response to an acoustic stimulus in the ear canal, a wave propagates on the BM in the forward direction, i.e., from the base toward the apex of the cochlea (in the $+x$ direction; see Fig. 1 A). The magnitude of the wave peaks at a location that depends on the stimulus frequency, called the "best place". Because the wave speed (from tens of m/s to a few m/s) is much smaller than the speed of sound in water, this wave is commonly called the "slow forward traveling wave". Despite the common use of DPOAEs, questions still remain as to how DPs propagate in the reverse direction ($-x$ direction) from their generation sites to the ear canal. Two main hypotheses, shown in Fig. 1, B and C, have
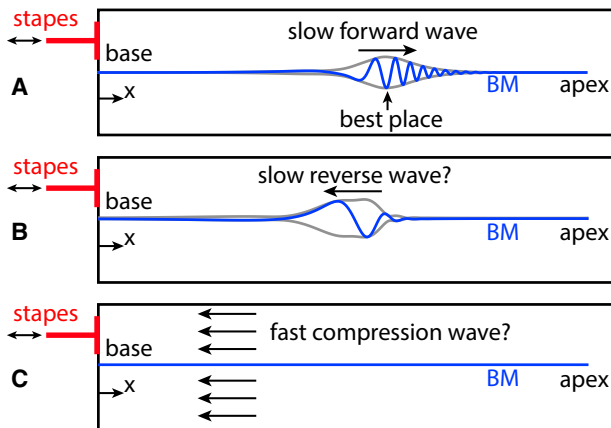
FIGURE 1 Schematics of wave propagation in the cochlea. (A) Here we show response to an acoustic stimulus. Given here are proposed hypotheses for DP propagation as (B) slow reverse wave and (C) fast compression wave. BM, basilar membrane. To see this figure in color, go online.

been proposed for how DPs propagate: 1) as a slow reverse traveling wave along the BM (7,13) or 2) as a fast compression wave through the cochlear fluid (14,15). The fast compression wave is a longitudinal pressure wave that travels at the speed of sound in water (1500 m/s). A clear understanding of how DPs propagate within the cochlea is needed to improve the usefulness of DPOAE measurements in clinical and research settings.

In the slow wave theory, once the reverse traveling wave reaches the stapes, part of the DP wave is transmitted through the middle ear and into the ear canal where it can be measured as a DPOAE; the other part is reflected at the stapes and propagates as a slow forward wave. Early models (e.g., (16)) have shown that DPs are expected to propagate back to the stapes as slow traveling waves. However, measurements of the BM velocity at the DP frequency have not provided any direct evidence for slow reverse propagation. Ren (14) measured the DP in the BM velocity at multiple positions and found that the phase is consistent with a forward propagating wave even though the locations were hypothesized to be basal to the DP generation site (such that a slow reverse traveling wave was expected to be observed). These results were interpreted as evidence that the DP propagates as a fast compression wave in the cochlear fluid; according to this theory, the fast compression wave would be reflected at the stapes, which would launch a slow forward traveling wave. Simultaneous measurements of the DP at the stapes and two longitudinal BM positions in a subsequent article (15), and of the phase of the stapes vibrations relative to the BM vibrations at the DP frequency (17), were interpreted as further supporting the theory of fast compression waves.

However, it has been argued that the BM measurements of Ren and co-workers (14,15,17) might be within the region in which DPs are generated, which might complicate the interpretation (18). Indeed, theoretical efforts using one-duct models that only allow slow wave components (19–23) have demonstrated that these measurements are not necessarily inconsistent with the reverse traveling wave theory. Analysis using 1D nonlinear cochlear models have shown that DP generation extends over a wide region that extends toward the base for low f_2/f_1 ratios and moderate to high stimulus levels (20,22). Similarly, Sisto et al. (21) found that a region dominated by a forward traveling wave is expected whenever DP generation occurs over a wide region and/or the stapes has high reflectivity. Using a more realistic 2D one-duct cochlear model, Vetešník and Gummer (23) also explained the observation of forward traveling waves in (14,15,17) by the fact that the measurement locations might be located at or apical to the DP generation sites. In (19), DP propagation was studied using a nonlinear 3D cochlear model with the stimulus applied from within the cochlea instead of from the stapes; decomposition of the DP response into forward and reverse traveling waves showed that the response is dominated by a slow reverse traveling wave from around the f_2 best place to the stapes. de Boer et al. (24) measured DPs with a frequency well below the characteristic frequency (CF) of the measurement location and observed that whereas a forward traveling wave is observed when f_2 is near CF, a slow reverse traveling wave is observed when f_2 is lower than CF.

It is more advantageous to investigate DP propagation by measuring the intracochlear pressure instead of the BM response because pressure measurements can detect both the compression and slow traveling wave modes (25). Many theoretical articles have investigated intracochlear fluid mechanics in response to a pure tone (26–28). In particular, it is well understood that the fluid pressure is truly 3D close to the peak of the traveling wave in the short-wave region (i.e., in the region where the wavelength of the slow wave is small compared to the height of the cochlear ducts), whereas it is ~1D closer to the base, in the long wavelength region (i.e., in the region where the wavelength is large compared to the duct height) (29). Using novel pressure sensors (30), Olson characterized the in vivo response of the intracochlear fluid pressure to a pure tone (31,32). More recently, Dong and Olson (11,25) and Dong (33) measured the intracochlear pressure DP in response to a two-tone stimulus. When the CF of the measurement location is near the f_2 and f_{DP} best places, it was found that the DP pressure in the scala tympani (ST) is localized around the BM (11). In these measurements, the amplitude of the DP decreases at a similar rate as a pure tone of the same frequency with increasing distance from the BM; such a decay of the amplitude is at odds with the compression wave theory. Subsequent measurements in (25) provided strong evidence for the reverse traveling wave hypothesis, because the ear canal pressure is delayed relative to the intracochlear DP for f_2 frequencies that are significantly lower than the CF of the measurement location. Recent measurements of the pressure at two basal intracochlear locations

by Dong (33) confirmed that the DPs are generated near the f_2 best place and have both forward and reverse traveling wave components.

Despite the critical role of the intracochlear fluid in the propagation of the DP from its generation site to the stapes, no model has investigated the DP intracochlear pressure. It is challenging to measure the fluid pressure at multiple longitudinal locations in vivo. Because of the presence of multiple waves (slow reverse wave, slow forward wave, and fast wave), measurements at one or two longitudinal location(s) are difficult to interpret. Furthermore, although the ST fluid pressure has been measured in active cochleae (32), measurements of the fluid pressure in the scala media have only been possible in passive cochleae (34). Hence, a model is needed to clarify how DPs vary spatially within the cochlear fluid pressure. The objective of this work is to analyze the generation of DPs and to quantify the relative contributions of slow reverse waves and fast compression waves to DP propagation. Because cochlear fluid mechanics is 3D and includes fast and slow modes, these physiological questions are addressed using a physiological two-duct 3D model of the cochlea. Furthermore, the active feedback mechanism is based on a realistic model of OHC biophysics that includes nonlinear MET channels and linearized somatic electromotility. Responses of the fluid pressure in response to a two-tone stimulus are compared to published in vivo measurements for model validation. Spatial variations of the total fluid pressure and of the different pressure modes are analyzed to gain a more complete understanding of how DPs propagate from their generation location out of the cochlea.

METHODS

Cochlear model

A model of the gerbil cochlea was developed because measurements of the intracochlear DP pressure have been performed in this species (e.g., (11,25,33)). This model is adapted from the physiologically based 3D model of the guinea pig presented in a series of articles (35–37). The model is based on the finite element method and includes mechanical, acoustic, and electrical physics to represent the cochlea (see Fig. 2 for a schematic and the Supporting Material for a brief description of the model equations). The model includes a realistic model of the organ of Corti geometry (see the Supporting Material) and micromechanics, with degrees of freedom for the tectorial membrane (TM) (both a bending and shear displacement, as described in (38)) and for the BM; the BM transverse displacement is assumed to be given by $u_{bm}(x,y,t) = U_{bm}(x,t)\psi(y)$, where $\psi(y)$ is a half-sinusoid and $U_{bm}(x,t)$ is the BM displacement at the center of the cross section. Longitudinal coupling is included for both the BM and TM, as described in (39).

Fluid model. The geometry of the cochlear ducts is described by a straight box model with two ducts. Although a two-duct model is not needed to predict the BM response because the BM is only excited by the pressure difference across the cochlear partition, a two-duct model is required to obtain realistic simulations of the intracochlear fluid pressure. The cochlear fluid is assumed to be incompressible (which implies that the speed of the fast wave is infinite in the model). Furthermore, fluid viscosity is ignored; the effect of viscosity is lumped into the damping parameters of the structural model. The fluid at the oval window is coupled to the stapes via the linearized Euler equation, the round window is modeled
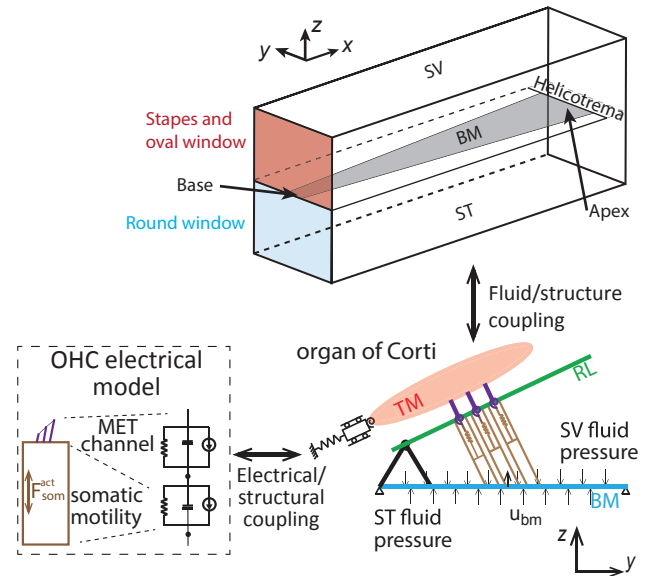

FIGURE 2 Schematic of the cochlear model fluid, structural, and electrical domains. TM, tectorial membrane; RL, reticular lamina; BM, basilar membrane; ST, scala tympani; SV, scala vestibuli; OHC, outer hair cell; MET, mechanoelectrical transduction. F_{som}^{act} is the force applied by the OHCs on the RL and BM, and U_{bm} is the displacement of the BM. To see this figure in color, go online.

as a pressure release, and all other bony walls of the cochlea are rigid. As introduced in (40), the pressure, $P_T(x,y,z,t)$, is decomposed into radial mode shapes so that a 2D mesh can give a 3D solution:

$$P_T(x, y, z, t) = \sum_{m=0,2,4...}^{M} P_T^{(m)}(x, z, t)\phi_m(y),$$

$$\text{where } \phi_m(y) = \cos\left[\frac{m\pi(y + w/2)}{w}\right], \quad (1)$$

where x, y and z are the distance in the longitudinal (from the stapes), radial (from the center of the duct), and transverse directions (from the BM), respectively; t is the time; m is the mode number; $P_T^{(m)}$ is the modal amplitude of the mth mode; $\phi_m(y)$ is the mth mode shape; and w is the width of the cochlear duct. Radial symmetry is assumed so that only the even modes are necessary. Unlike in previous works (e.g., (37,38)) that only used the first three modes, the first 25 even modes ($M = 48$) are included in this work to give a more accurate calculation of the 3D pressure (see the Supporting Material for a convergence study). The fluid elements directly above (in the scala vestibuli, SV) and below (in the ST) the cochlear partition are coupled to the BM displacement. To determine the contributions of the slow traveling wave and fast compression wave, the pressure is decomposed into the sum of an antisymmetric part, P_{as}, and of a symmetric part, P_s (26):

$$P_{as}(x, y, z, t) = \frac{1}{2}[P_T(x, y, z, t) - P_T(x, y, -z, t)], \quad (2)$$

$$P_s(x, y, z, t) = \frac{1}{2}[P_T(x, y, z, t) + P_T(x, y, -z, t)]. \quad (3)$$

Because the SV and ST dimensions are identical in the model and the fluid is only coupled to the BM, only the antisymmetric component interacts with the BM. Hence, the antisymmetric and symmetric components correspond to the slow traveling wave and fast compression wave, respectively (26,34).

Because the round window is modeled as a pressure release, the symmetric and antisymmetric components must be equal at $x = 0$.

OHC electrical model. The model uses the same electrical domain model as developed in (37). The MET current, I_{MET}, is modeled with the Boltzmann function:

$$I_{MET}\left(\theta_{hb/rl}\right) = G_{hb}^{max}\Delta V_{hb}^0\left[\frac{1}{1 + \exp\left[-\dfrac{L_{hb}\theta_{hb/rl} - X_0}{\Delta X}\right]} - P_0^s\right], \tag{4}$$

where $\theta_{hb/rl}$ is the angular deflection of the hair bundle, G_{hb}^{max} is the saturating hair bundle MET conductance, P_0^s is the resting open probability of the MET channel, ΔV_{hb}^0 is the resting value of the difference between the scala media potential and intracellular OHC potential, L_{hb} is the length of the hair bundles, and X_0 and ΔX are constant displacements. Somatic electromotility is modeled by the following equations:

$$i_{ohc}(t) = G_m\Delta\phi_{ohc}(t) + C_m\frac{d\Delta\phi_{ohc}(t)}{dt} - \varepsilon_3\frac{du_{ohc}^{comp}(t)}{dt}, \tag{5}$$

$$f_{ohc}(t) = K_{ohc}u_{ohc}^{comp}(t) + \varepsilon_3\Delta\phi_{ohc}(t), \tag{6}$$

where i_{ohc}, $\Delta\phi_{ohc}$, and f_{ohc} are the perturbations in the somatic current, transmembrane potential, and electromechanical force from their resting values, respectively; u_{ohc}^{comp} is the OHC compression; G_m and C_m are the basolateral conductance and capacitance, respectively; ε_3 is the electromechanical coupling coefficient; and K_{ohc} is the OHC stiffness.

Calibration of the cochlear model. To accurately model the response of the gerbil cochlea, it was necessary to adjust many of the parameters from the guinea pig model of (37). When possible, parameters, such as the anatomical geometry or the mass of the TM in bending and shear, were chosen based on available measurements (e.g., (41,42)). Remaining parameters were either kept at the value previously used in (37) or adjusted manually so that the model response approximated available measurements for the response of the gerbil cochlea to a pure tone (43–45). A complete list of the model parameters can be found in the Supporting Material.

Boundary conditions at the stapes. To enable easy modification of the boundary conditions at the stapes, the stapes was modeled as a one-degree-of-freedom system instead of using a more realistic model of middle ear. The response of the coupled cochlea-stapes system is obtained by applying a force on the stapes. The amplitude of the force was converted to an ear canal pressure in dB SPL (sound pressure level, using 20 μPa as the reference pressure) by examining the amplitude of the pressure at the stapes in the SV in response to a pure tone; the ear canal pressure was assumed to be 30 dB lower than the SV pressure at the stapes, based on measurements from (32,46).

Distortion product simulations. For this work, we consider the low-side cubic DP at the frequency $f_{DP} = 2f_1 - f_2$, where f_1 and f_2 (in which $f_2 > f_1$) are the primary frequencies that comprise the two-tone stimulus. Only equilevel primaries are considered for all results shown in this article. As in our recent work (37), simulations of the nonlinear response are run in the time-domain using the state space approach described by Elliott et al. (47). To avoid any broadband excitation of the model at the stimulus onset, the onset of the two primaries had a raised cosine envelope with a rise time of 1 ms. The response at the primary and DP frequencies was obtained using MATLAB's (The MathWorks, Natick, MA) built-in FFT function. In addition to the distortion source, DPOAEs are also known to have a reflection source component due to coherent reflection by inhomogeneities near the DP best place (48). To simplify the analysis, a smooth cochlear model is employed and only the distortion source component is investigated.

Decomposition of the slow wave into reverse and forward wave components

Following the approach from (19), the model response at the DP frequency is decomposed into approximate forward and reverse traveling wave components. The procedure involves taking the spatial Fourier transform of the antisymmetric pressure at the DP frequency, $P_{as}^{DP}(x,y,z)$, into the wavenumber domain:

$$\tilde{P}_{as}^{DP}(k, y, z) = \int_{-\infty}^{\infty} P_{as}^{DP}(x, y, z)e^{-ikx}dx, \tag{7}$$

where k is the wavenumber and $\tilde{P}_{as}^{DP}$ is the wavenumber spectrum of P_{as}^{DP}. The wavenumber spectrum is then separated into a forward wave component, $\tilde{P}_{as}^{DP,f}$, and a reverse wave component, $\tilde{P}_{as}^{DP,r}$ by assuming that for $k \neq 0$:

$$\begin{aligned}
\tilde{P}_{as}^{DP,f}(k, y, z) &= \tilde{P}_{as}^{DP}(k, y, z) \text{ if } k > 0, \\
\tilde{P}_{as}^{DP,r}(k, y, z) &= \tilde{P}_{as}^{DP}(k, y, z) \text{ if } k < 0, \\
\tilde{P}_{as}^{DP}(k, y, z) &= \tilde{P}_{as}^{DP,f}(k, y, z) + \tilde{P}_{as}^{DP,r}(k, y, z) \text{ for any } k \neq 0.
\end{aligned} \tag{8}$$

Once the two components are found in the wavenumber domain, the value of the forward and reverse wave components in the spatial domain, $P_{as}^{DP,f}$ and $P_{as}^{DP,r}$, are given by the inverse Fourier transform of the two components in the wavenumber domain:

$$P_{as}^{DP,f}(x, y, z) = \int_{-\infty}^{\infty} \tilde{P}_{as}^{DP,f}(k, y, z)e^{ikx}dk, \tag{9}$$

$$P_{as}^{DP,r}(x, y, z) = \int_{-\infty}^{\infty} \tilde{P}_{as}^{DP,r}(k, y, z)e^{ikx}dk. \tag{10}$$

Equation 8 does not specify the values of the forward and reverse components at $k = 0$; these values were found by making sure that the ratio of $P_{as}^{DP,f}$ to $P_{as}^{DP,r}$ at $x = 0$ is equal to the stapes reflection coefficient, using the approach described in the Supporting Material.

RESULTS

Pure tone response

The response of the model to a pure tone is first discussed. At a longitudinal position x and frequency ω, the gain of the BM velocity relative to the stapes velocity is defined as:

$$G_{bm}(x, \omega) = \frac{v_{bm}(x, \omega)}{v_s(\omega)}, \tag{11}$$

where v_{bm} (given by $i\omega U_{bm}$, in which U_{bm} is the displacement of the BM at the center of the BM) and v_s are the velocities of the BM and stapes, respectively. In Fig. 3, A and B, the magnitude of the gain is normalized by the low SPL value of the gain at CF (to aid in comparison with experimental data) and is plotted as a function of frequency at two longitudinal locations (chosen to match the positions of measurements of the BM response in (43) and (44)) in Fig. 3. At both positions, the sharpness of tuning seen in the low SPL results is similar to what is seen in the experimental data; furthermore,
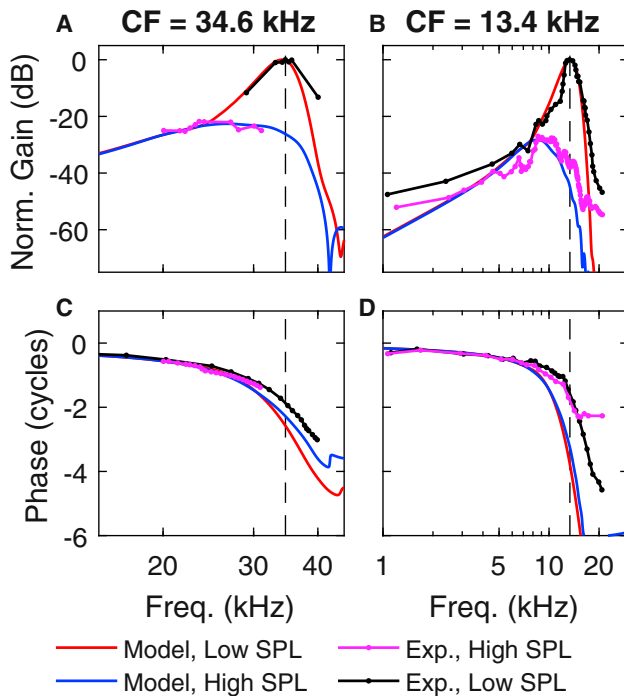
FIGURE 3 Comparison of BM pure tone response for model and experimental data was taken from (43,44). (A and B). Gain of the BM velocity relative to the stapes velocity. The model gain was normalized by the gain predicted by the model at low SPL at CF (55 dB in A and 60 dB in B); the experimental gain was normalized by the gain seen at CF in the low SPL experiments (53 dB in A and 49 dB in C). (C and D) Phase of the BM velocity relative to the stapes velocity. (A and C) Experimental data from (44) is given. (B and D) Experimental data from (43) is given. (A and C) Results for 30- and 90 dB SPL and 50- and 90 dB SPL stimuli, respectively. (B and D) Results for 30- and 100 dB SPL stimuli. The vertical black dashed lines denote CF. To see this figure in color, go online.

the gain of the low SPL to high SPL model results (22.6 dB for CF = 34.6 kHz and 28.5 dB for CF = 13.4 kHz) is similar to what is seen in the experimental data. This is a result of an effort during the calibration process to match the experimental gain and tuning sharpness seen in these experiments. At the more basal position (CF = 34.6 kHz), the model high SPL results peak at 26 kHz and the experimental high SPL results peak at 24–25 kHz, whereas, at the more apical position (CF = 13.4 kHz) both model and experimental high SPL results peak at 8–9 kHz. In Fig. 3 C, the model phase decreases at almost the same rate as the experimental results. In Fig. 3 D, both the low and high SPL model phases decrease at a faster rate than the experimental data. Model and experimental results for the fluid pressure are compared in Fig. S4.

Two-tone response

Response on the basilar membrane

The spatial response of the BM to a two-tone stimulus is shown in Fig. 4 for two primary frequency ratios (f_2/f_1 = 1.05 in Fig. 4, A and C; f_2/f_1 = 1.35 in Fig. 4, B and D).
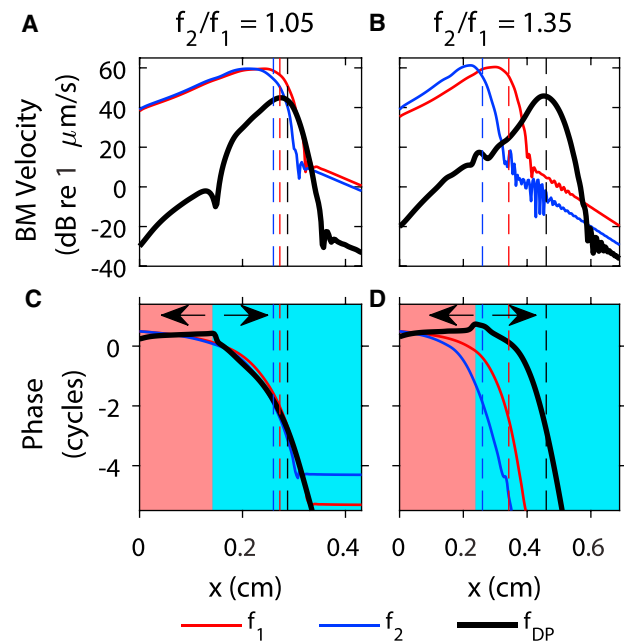

FIGURE 4 (A–D) BM velocity of the DP and primaries as a function of longitudinal position for primary frequency ratios, f_2/f_1, of 1.05 and 1.35, f_2 = 24 kHz, and primary stimuli levels of 80 dB SPL. The vertical dashed lines from left to right indicate the f_2, f_1, and f_{DP} best places, respectively. The red shading indicates when the phase has a positive slope and the cyan shading indicates when the phase has a negative slope. To see this figure in color, go online.

As in most of the intracochlear DP pressure measurements (11,33), the level of the primaries was chosen to be 80 dB SPL. For both primary ratios, the f_1 and f_2 responses have peaks of similar amplitude (Fig. 4, A and B) and the primaries peak at a location basal to their best places due to the relatively high stimulus level of the two primaries. The DP peaks slightly basal to its best place for f_2/f_1 = 1.05 and at its best place for f_2/f_1 = 1.35. Two different regions can be identified in the plot of the phase at the DP frequency (Fig. 4, C and D): in the basalmost red-shaded region, the slope of the phase is positive, such that DP propagation is dominated by a slow reverse traveling wave; in the blue-shaded region, the phase slope is negative, which indicates that DP propagation is dominated by a slow forward traveling wave. For f_2/f_1 = 1.05, this transition from reverse to forward wave propagation occurs basal to the f_2 best place, whereas for f_2/f_1 = 1.35, this transition occurs approximately at the f_2 best place.

Spatial variations in intracochlear pressure

Because the cochlear fluid plays a critical role in the propagation of both slow and fast waves, the spatial variations of the pressure were analyzed (Fig. 5). In this work, unless stated otherwise, pressure magnitudes are presented in dB SPL with a reference pressure of 20 μPa. In Fig. 5, C–F, the pressure magnitude is plotted as a function of x and z for positions within the plane shown in Fig. 5 A. To help understand the DP
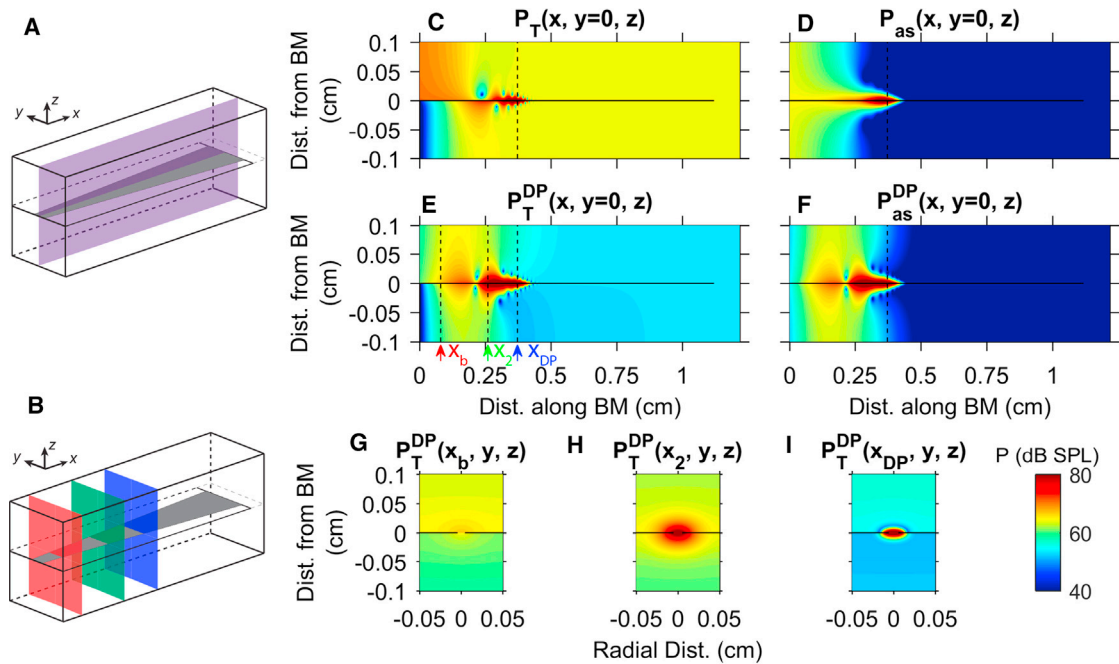
FIGURE 5 (*A* and *B*) Box models are given with planes indicating where the pressure is shown in (*C–F*) and (*G–I*), respectively. Total and antisymmetric pressure component magnitudes for pure-tone (*C* and *D*) and two-tone stimuli are given (*E* and *F*). Cross sections of pressure magnitude at several positions are given (*G–I*). The pure-tone stimuli (*C* and *D*) was at 16 kHz and 40 dB SPL and the two-tone stimuli (*E–I*) has $2f_1 - f_2 = 16$ kHz, primary frequency ratio $f_2/f_1 = 1.20$, and primary stimulus level of 80 dB SPL. The horizontal black line represents the cochlear partition. The vertical dashed line in (*C*), (*D*), and (*F*) denotes the 16 kHz best place. The arrows and vertical dashed lines on (*E*) from left to right denote the positions shown in (*G–I*), respectively. The three positions shown in (*G–I*) are an arbitrarily chosen basal position, $x_b = 0.08$ cm; the f_2 best place ($x_2 = 0.26$ cm); and the DP best place ($x_{DP} = 0.37$ cm), respectively. To see this figure in color, go online.

response in response to a two-tone stimulus, the pure tone response is first presented in Fig. 5, *C* and *D*; the stimulus frequency was chosen to match the frequency of the DP (16 kHz) seen in the two-tone results. As described in the Methods, the total pressure was decomposed into its symmetric and antisymmetric components, which correspond to the fast and slow waves, respectively. The spatial variations of the fluid pressure in response to a pure tone are similar to what has been previously observed in 3D two-duct cochlear models (e.g., (27,28,49)). For brevity and because it is nearly uniform throughout both cochlear ducts, the symmetric pressure is not shown; the amplitude of the symmetric component corresponds to the total pressure amplitude in the most apical region near the helicotrema where the antisymmetric pressure has a low amplitude. The lobes seen in the total pressure close to the BM from $x = 0.2$ to 0.5 cm (Fig. 5 *C*) are due to wave interference between the antisymmetric (shown in Fig. 5 *D*) and symmetric components. Similar notches in the pressure have been observed experimentally (e.g., (11,25)). At the base, in the long-wave region, the antisymmetric pressure is ~1D, whereas it becomes more localized and 3D around the BM closer to the 16 kHz best place, in the short-wave region.

The fluid pressure at the DP frequency in response to a two-tone stimulus shares some similarities with the pure tone response. In addition to the pressure as a function of

x and *z* (Fig. 5, *E* and *F*), the DP results include the pressure as function of *y* and *z* (Fig. 5, *G–I*) at three longitudinal locations identified by the three planes shown in Fig. 5 *B*. The DP antisymmetric pressure is 1D in the long wave region and 3D in the short wave region (Fig. 5 *F*). As with the pure tone, the DP symmetric pressure is nearly uniform throughout the cochlear ducts and the amplitude of the symmetric component corresponds to the total pressure in the apical regions. However, some notable differences between the pure tone and DP responses can be observed. The magnitude of the pure-tone symmetric pressure is much higher than the DP symmetric pressure, such that lobes of minimum pressure close to the BM are not observed in the total DP response in Fig. 5 *E*. Furthermore, a region of minimum magnitude is observed in both the total and antisymmetric DP pressure at ~$x = 0.20$ cm; this minimum, not observed in the pure tone response, relates to the minimum or notch in the BM response in Fig. 4 and will be discussed further below. Model simulations for the spatial variations of the DP pressure are compared to experimental results in Fig. S6.

Effects of varying f_2 on DP propagation at fixed location

Although cochlear models easily provide the response for a given frequency at all positions, it is much easier to measure

the response at a fixed position and sweep frequency in an experiment. In a scale-invariant cochlea, these two methods should be equivalent (24). In Fig. 6, the effects of varying f_2 at a fixed position (20 kHz best place) for different f_2/f_1 ratios are shown. This scheme is commonly used in experiments (e.g., (15,17,24,25,33)) to investigate intracochlear DP response and propagation. The magnitude and phase of the ratio of the pressure in the ST close to the BM to the pressure in the SV close to the stapes is compared with recent measurements from Dong (33). Due to variability in the experimental results, only the pressure ratios are compared here.

As in the measurements (Fig. 6 B), the peak of the DP response shifts to higher frequency as the frequency ratio is increased (Fig. 6 A); this is because the DP is approximately tuned to its own CF and the x axis is f_2. Although the magnitude of the pressure ratio agrees well with experiments for $f_2/f_1 = 1.25$ and 1.35, it is ~10 dB higher than in the experiments for $f_2/f_1 = 1.05$, and 13 dB lower than in the experiments for the pure tone results. Both in the model and the experiments, the DP response for $f_2/f_1 = 1.05$ has similar tuning as the pure tone response, whereas it has broader tuning at higher ratios. In contrast to the experimental results,
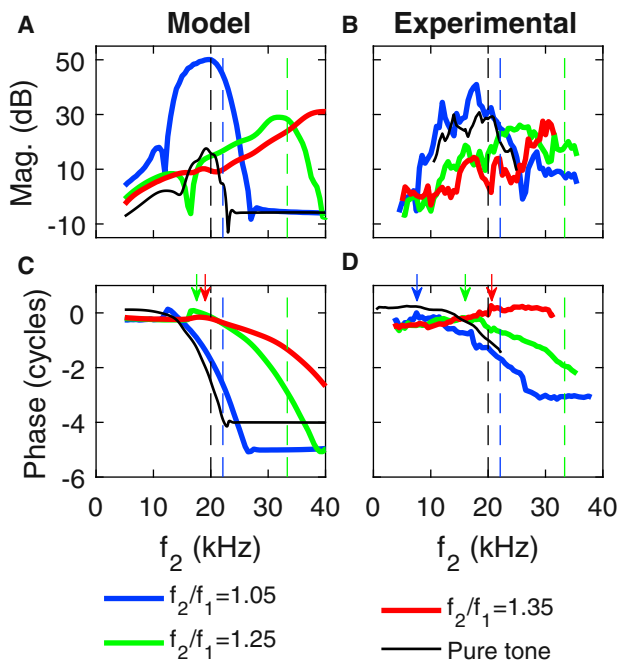
the curves obtained with the model are smooth, possibly because the reflection from the DP best place due to cochlear roughness is not taken into account in the model. Similar to the lobes in Fig. 5 C, the pure tone shows notches in amplitude at ~14 and 23 kHz that are due to interactions between the symmetric and antisymmetric pressure. For $f_2 > 30$ kHz, the magnitudes of the $f_2/f_1 = 1.05$ DP and pure tone are almost constant, indicating that the total pressure is converging to the symmetric pressure.

The phase of the ST pressure at the 20 kHz best place relative to the SV phase at the stapes, shown in Fig. 6, C and D, is particularly important for determining how DPs propagate. Two frequency regions can be identified, both in the case of the model simulations (Fig. 5 C) and the experiments (Fig. 5 D). At low frequency, the slope of the phase tends to be shallow; it is positive (indicating a slow reverse traveling wave) for $f_2/f_1 = 1.25$ and 1.35, although both positive and negative slopes are observed for $f_2/f_1 = 1.05$ (indicating wave interference). At higher frequencies, a negative slope that progressively becomes steeper (indicating a forward traveling wave that slows down) is observed. For $f_2/f_1 = 1.05$ and 1.25, the region dominated by the forward wave starts at frequency f_2 below the CF of the location; for $f_2/f_1 = 1.35$, this frequency region starts approximately when $f_2 = CF$ in the model simulations, although a forward traveling wave is not clearly observed for the frequencies that were measured in the experiment. As in the pure tone response, the phase predicted by the model has a steeper slope when $f_{dp} \approx CF$ than in the experiment.

Forward and reverse wave components

To further analyze DP propagation, the DP fluid pressure was first decomposed into its symmetric and antisymmetric components and then the antisymmetric pressure was decomposed into forward and reverse components. As required by the pressure release boundary condition at the round window, the symmetric pressure equals the antisymmetric pressure at $x = 0$ (Fig. 7 A); furthermore, the symmetric pressure is nearly constant. As expected, the phase lag of the forward waves increases as it propagates forward whereas the phase lag of the reverse wave increases as it propagates toward the stapes (Fig. 7 B). This confirms that the wave decomposition method is able to separate the total response into forward and reverse wave components. Next to the stapes (at $x = 0$), the reverse traveling wave is >10 dB higher than the symmetric pressure, implying that emissions are dominated by the slow reverse traveling wave. The decomposition is particularly useful in interpreting the magnitude and phase of the total response. For example, the reverse wave has a higher magnitude than the forward wave basal to $x = 0.20$ cm in Fig. 7 A; hence, the total response is dominated by the reverse wave at the base and the phase of the total response has a positive slope

FIGURE 6 Shown here is the magnitude (*A* and *B*) and phase (*C* and *D*) of the ratio of the DP pressure in the ST, 10 μm from the BM, to the DP pressure in the SV next to the stapes (halfway between the BM and the top of the SV) as a function of f_2. (*A* and *C*) Model results are given. (*B* and *D*) Measurements from (33) are shown. All results are at the 20-kHz best place. Model and experimental DPs had primary stimuli levels of 80 dB SPL. For reference, the response to a pure tone with a 40 dB SPL stimulus is also shown. The vertical dashed lines indicate f_2 when f_{DP} (or f for the pure tone) corresponds to the CF of 20 kHz. Vertical arrows mark the transition from reverse to forward waves. To see this figure in color, go online.
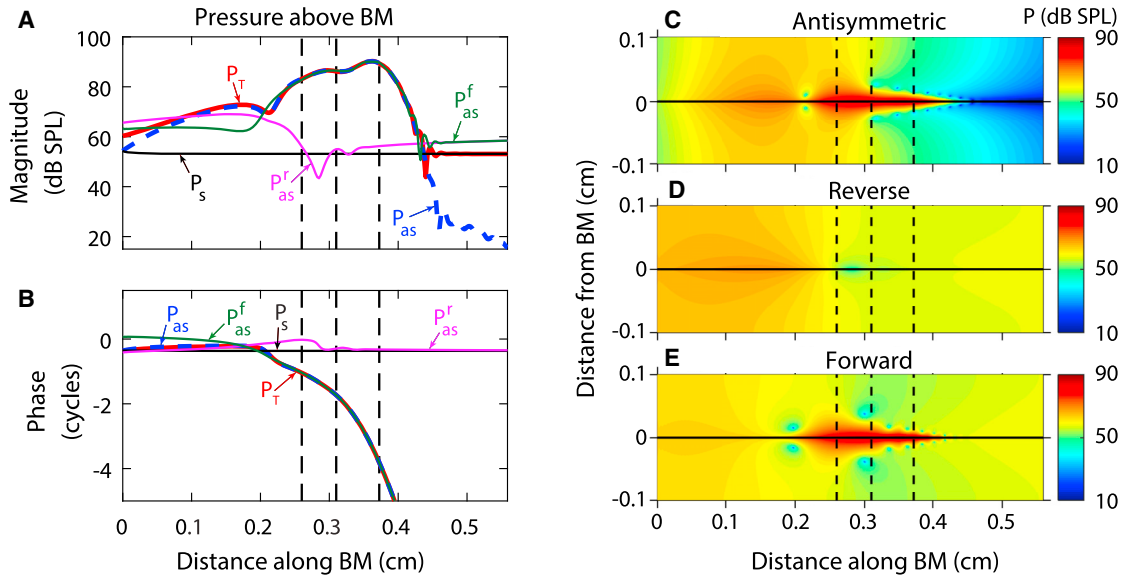
FIGURE 7 Given here is decomposition of the DP pressure for equilevel primaries of 80 dB SPL with $f_2/f_1 = 1.20$ and $f_2 = 24$ kHz. (A and B) Magnitude and phase of the total pressure, P_T; symmetric pressure, P_s; antisymmetric pressure P_{as}; forward wave component of the antisymmetric pressure, P_{as}^f; and reverse wave component of the antisymmetric pressure, P_{as}^r are all taken directly above the BM in the SV. (C–E) Magnitude of the antisymmetric pressure (C), reverse wave component of antisymmetric pressure (D), and forward wave component of antisymmetric pressure (E) are shown. The vertical dashed lines indicate, from left to right, the f_2, f_1, and f_{DP} best places. To see this figure in color, go online.

(Fig. 7 B). Near $x = 0.20$ cm, both forward and reverse waves have similar magnitudes but phases that differ by nearly half a cycle. This results in wave interference and a minimum in the total and antisymmetric pressure (Fig. 7, A and C). Apical to $x = 0.20$ cm, the magnitude of the reverse wave decreases and the magnitude of the forward wave matches the total response almost exactly (Fig. 7 A); no reverse traveling waves are expected to be generated near or apical to the DP best place and thus, the response should be dominated by the forward traveling wave. Because the response is dominated by a forward wave, the phase of the total response has a negative slope. Because the DP reverse traveling wave originates basal to the region of amplification, the reverse wave is similar to the pure tone response (if the phase is negated). Furthermore, the phase accumulation of the reverse wave from the generation site to the stapes is very limited because the wavelength of a slow wave (both in the case of a forward or reverse wave) is large at locations basal to the best place.

For the case shown in Fig. 7 B, the phase delay of the forward and reverse waves relative to the position of maximum phase ($x = 0.16$ cm) can be calculated as

$$\tau_\phi(x) = \frac{\phi_{DP}(x = 0.16) - \phi_{DP}(x)}{f_{DP}}, \quad (12)$$

where τ_ϕ is the phase delay, and ϕ_{DP} is the phase of the antisymmetric pressure at f_{DP}. The phase delay for the forward wave between $x = 0.16$ cm and the DP best place ($x = 0.37$ cm) is 0.22 ms, corresponding to an average phase

velocity of ~9 m/s. The phase delay for the reverse wave between $x = 0.16$ cm and $x = 0$ is 0.014 ms, corresponding to an average phase velocity of ~112 m/s. Thus, the reverse wave propagates back to the base from the generation region ≈ 12 times faster than the forward wave propagates from the generation region to the DP best place.

Examining the spatial variations of the pressure in x and z (Fig. 7, C–E) yields similar findings to Fig. 7 A. Like the antisymmetric pressure, the forward wave pressure is localized around the BM near the primary and DP best places. The reverse wave appears less localized around the BM and the pressure is nearly 1D because the reverse wave has a maximum amplitude in the long wave region for the DP frequency. Furthermore, the zone of low pressure in the antisymmetric pressure close to the BM at $x \approx 0.22$ cm is due to wave interference between the forward and reverse waves. Additional results for the effects of varying the stapes reflection coefficient, R_{st}, and the primary frequency ratio, f_2/f_1, on the forward and reverse waves are shown in Figs. S9 and 10 and in Movies S1 and S2. Observation of the reverse wave, in particular, makes it possible to visualize how the DP generated near the f_2 best place progressively propagates toward the stapes.

DISCUSSION

Strengths and limitations of this modeling approach

The propagation of DPs is examined in this article using a physiologically based model that is more realistic than in

previous theoretical studies (19–23): our model includes a detailed representation of OHC biophysics, with nonlinear MET channels and linearized somatic electromotility; furthermore, the fluid model is based on a two-duct 3D model. Although 3D cochlear models have previously examined intracochlear fluid mechanics in response to a pure tone (26–28), intracochlear fluid mechanics is analyzed, to our knowledge, for the first time in response to two-tone stimuli in this work. Note, however, that the fluid is only coupled to the BM in this model. Direct coupling of the ST fluid to the TM, as in some recent models (50–52), might better represent intracochlear fluid mechanics; however, the coupling considered in this article is simpler to analyze, because decomposition of the pressure into symmetric and antisymmetric components makes it possible to identify the slow and fast waves. To get insight into how DPs propagate, the slow wave component of the fluid pressure was decomposed into forward and reverse waves using the method previously proposed for the decomposition of the BM velocity by de Boer et al. (19).

The model was calibrated such that the gain and sharpness of tuning in response to a pure tone are similar to in vivo measurements of the BM response to sound in the gerbil cochlea (43,44). Because of the existence of extensive sets of experimental data, models have been previously developed by other researchers for the gerbil cochlea (28,52). As in some previous studies (28), we found that matching the phase of the model pure tone response to measurements was more challenging than matching the magnitude. Due to the discrepancy between model and experiments in the phase of the pure tone response, the slope of the phase of the DP response when $f_{dp} \approx$ CF is steeper than in the measurements; furthermore, the magnitude of the DP pressure decays at a faster rate as the location moves away from the BM than in experiments (see Fig. S6, A–C).

Another limitation of this research is that all results are based on a smooth cochlear model. Because of the absence of cochlear roughness, the model only includes the distortion source, i.e., DPOAEs are only generated due to nonlinear distortion in the region where the two primaries interact. However, it is well known that DPOAEs also include a reflection source component that is commonly hypothesized to be generated due to coherent reflection by putative inhomogeneities close to the peak of the DP response (48). The presence of another source of DPOAE would complicate the analysis because more reverse wave components might be expected. The reflection source, which plays a particularly significant role in the case of the $2f_2 - f_1$ DP, will be analyzed in future work.

Analysis of the spatial variations of the DP fluid pressure

In a two-duct model, the response of the fluid pressure is the superposition of a symmetric, fast wave mode and of an antisymmetric, slow wave mode that propagates on the BM due to the fluid/structure interaction between the BM and the fluid. The presence of both modes is predicted both in the case of the pure tone response and of the DP response; furthermore, the main properties of the two modes are the same in the pure tone and DP responses. Because we use a rectangular geometry for the two ducts, the fast compression mode is nearly uniform throughout the cochlear ducts (29) (Figs. 5, 7, and S6). The properties of the slow wave mode depend on the local wavelength of the traveling wave. Close to the stapes, the wavelength is long, such that the pressure is 1D and varies only with longitudinal position with little phase accumulation. As the wave approaches its best place, the wavelength becomes shorter and the wave slows down, resulting in more phase accumulation. In this short wave region, the pressure becomes more 3D and localized around the BM. Both in model simulations and in experiments (11,33), the fluid pressure in the ST decays exponentially as the measurement location is moved away from the BM when $f_{dp} \approx$ CF. This is because the symmetric pressure (which is nearly uniform) has a much smaller amplitude than the antisymmetric pressure (Fig. 5). Furthermore, the DP pressure decays at a similar rate as a pure tone pressure of the same frequency (Fig. S6), as observed experimentally (11).

The propagation of DPs can be represented by the schematics of Fig. 8 (which is an extension of Fig. 12 from Shera and Guinan (13)). In response to a two-tone stimulus, the two primaries propagate along the BM. A DP is generated due to nonlinear distortion in the region where the response to both primaries has a sufficiently high amplitude. According to our results, this DP propagates as a slow reverse wave toward the stapes and as a slow forward wave toward the helicotrema. As the forward wave approaches the DP best place, the forward wave is amplified and slows down (such that the wavelength becomes shorter); because of the short wavelength, the pressure is highly 3D and localized to the BM. The reverse wave
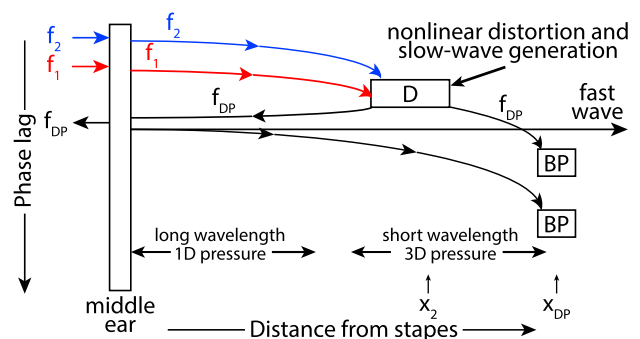

FIGURE 8 Schematics of DP propagation. The figure from (13) was redrawn and extended to include the fast wave, the long wavelength region, and the short wavelength wave region. Note that (D) is the distortion source; (BP) is the DP best place, x_{DP}; and (x_2) is the f_2 best place. To see this figure in color, go online.

propagates back to the base with little phase accumulation (because the wavelength is very long basal to the DP generation site); furthermore, because of the long wavelength, the pressure is ~1D. When this reverse wave reaches the stapes, part of this wave is transmitted by the middle ear (hence, a DPOAE is measured in the ear canal), whereas the other part is reflected by the stapes such that a slow forward traveling wave is generated. Simultaneously satisfying the boundary conditions at the stapes and round window requires the pressure to have a symmetric component, such that a DP fast wave is also generated. The DP fast mode is not directly generated by the OHCs because excitation of the fast wave by OHCs would require them to change volume. The fast wave instantly fills the cochlear ducts (because the fluid is assumed to be incompressible in the model), whereas the slow wave propagates forward with increasing phase accumulation as it approaches its best place.

Due to the presence of slow reverse and forward waves, a zone of wave interference is observed in the DP response of the BM velocity and fluid pressure. As found in previous BM DP modeling work (19–23) and experiments (14,15,17,33), by varying the stimulus parameters, the longitudinal position and the stapes reflectivity affects where and whether the forward or reverse wave dominates. Determining whether DPs propagate as a slow wave or a fast wave using only measurements at a couple of longitudinal locations is particularly challenging, due to the complicated influence of the stimulus parameters (such as the levels or frequency ratio of the primaries) and to the wave interference between the forward and reverse waves.

CONCLUSIONS

In this article, a two-duct 3D model with a realistic model of OHC biophysics was used to investigate how DPs vary spatially in the intracochlear fluid pressure. Some similarities with the pressure obtained in response to a pure tone are observed in the DP pressure. At positions at which the wavelength of the traveling wave is short, the DP pressure is 3D whereas it is ~1D closer to the base where the wavelength is long. Simulations demonstrate the presence of a fast compression wave, and a slow traveling wave that could be decomposed into forward and reverse traveling waves to help clarify DP propagation. At the base ($x = 0$), the fast compression and slow traveling waves are equal in amplitude, but the reverse traveling wave is substantially larger than the fast compression wave. Thus, emissions are dominated by the slow traveling wave mode.

SUPPORTING MATERIAL

Supporting Materials and Methods, nine figures, four tables, and two movies are available at http://www.biophysj.org/biophysj/supplemental/S0006-3495(17)35084-1.

SUPPORTING CITATIONS

References (53–64) appear in the Supporting Material.

REFERENCES

1. Robles, L., and M. A. Ruggero. 2001. Mechanics of the mammalian cochlea. *Physiol. Rev.* 81:1305–1352.

2. Ashmore, J., P. Avan, …, B. Canlon. 2010. The remarkable cochlear amplifier. *Hear. Res.* 266:1–17.

3. Kemp, D. T. 1978. Stimulated acoustic emissions from within the human auditory system. *J. Acoust. Soc. Am.* 64:1386–1391.

4. Lonsbury-Martin, B. L., and G. K. Martin. 1990. The clinical utility of distortion-product otoacoustic emissions. *Ear Hear.* 11:144–154.

5. Shera, C. A., J. J. Guinan, Jr., and A. J. Oxenham. 2002. Revised estimates of human cochlear tuning from otoacoustic and behavioral measurements. *Proc. Natl. Acad. Sci. USA.* 99:3318–3323.

6. Kemp, D. T. 2002. Otoacoustic emissions, their origin in cochlear function, and use. *Br. Med. Bull.* 63:223–241.

7. Kemp, D. T. 1986. Otoacoustic emissions, travelling waves and cochlear mechanisms. *Hear. Res.* 22:95–104.

8. Robles, L., M. A. Ruggero, and N. C. Rich. 1991. Two-tone distortion in the basilar membrane of the cochlea. *Nature.* 349:413–414.

9. Robles, L., M. A. Ruggero, and N. C. Rich. 1997. Two-tone distortion on the basilar membrane of the chinchilla cochlea. *J. Neurophysiol.* 77:2385–2399.

10. Cooper, N. P., and W. S. Rhode. 1997. Mechanical responses to two-tone distortion products in the apical and basal turns of the mammalian cochlea. *J. Neurophysiol.* 78:261–270.

11. Dong, W., and E. S. Olson. 2005. Two-tone distortion in intracochlear pressure. *J. Acoust. Soc. Am.* 117:2999–3015.

12. Fettiplace, R., and C. M. Hackney. 2006. The sensory and motor roles of auditory hair cells. *Nat. Rev. Neurosci.* 7:19–29.

13. Shera, C. A., and J. J. Guinan, Jr. 1999. Evoked otoacoustic emissions arise by two fundamentally different mechanisms: a taxonomy for mammalian OAEs. *J. Acoust. Soc. Am.* 105:782–798.

14. Ren, T. 2004. Reverse propagation of sound in the gerbil cochlea. *Nat. Neurosci.* 7:333–334.

15. He, W., A. Fridberger, …, T. Ren. 2008. Reverse wave propagation in the cochlea. *Proc. Natl. Acad. Sci. USA.* 105:2729–2733.

16. de Boer, E., C. Kaernbach, …, T. Schillen. 1986. Forward and reverse waves in the one-dimensional model of the cochlea. *Hear. Res.* 23:1–7.

17. He, W., A. Fridberger, …, T. Ren. 2010. Fast reverse propagation of sound in the living cochlea. *Biophys. J.* 98:2497–2505.

18. Shera, C. A., A. Tubis, and C. L. Talmadge. 2006. Four counter-arguments for slow-wave OAEs. *In* Auditory Mechanisms: Processes and Models. World Scientific, Singapore, pp. 449–457.

19. de Boer, E., A. L. Nuttall, and C. A. Shera. 2007. Wave propagation patterns in a "classical" three-dimensional model of the cochlea. *J. Acoust. Soc. Am.* 121:352–362.

20. Zhang, X., and D. C. Mountain. 2009. Distortion product emissions: where do they come from? *In* Concepts and Challenges in the Biophysics of Hearing: Proceedings of 10th International Workshop on the Mechanics of Hearing. N. P. Cooper and D. T. Kemp, eds. World Scientific Publishing, Singapore, pp. 48–54.

21. Sisto, R., A. Moleti, …, C. A. Shera. 2011. Distortion products and backward-traveling waves in nonlinear active models of the cochlea. *J. Acoust. Soc. Am.* 129:3141–3152.

22. Young, J. A., S. J. Elliott, and B. Lineton. 2012. Investigating the wave-fixed and place-fixed origins of the $2f_1 - f_2$ distortion product otoacoustic emission within a micromechanical cochlear model. *J. Acoust. Soc. Am.* 131:4699–4709.

23. Veteśník, A., and A. W. Gummer. 2012. Transmission of cochlear distortion products as slow waves: a comparison of experimental and model data. *J. Acoust. Soc. Am.* 131:3914–3934.

24. de Boer, E., J. Zheng, …, A. L. Nuttall. 2008. Inverted direction of wave propagation (IDWP) in the cochlea. *J. Acoust. Soc. Am.* 123:1513–1521.

25. Dong, W., and E. S. Olson. 2008. Supporting evidence for reverse cochlear traveling waves. *J. Acoust. Soc. Am.* 123:222–240.

26. Peterson, L. C., and B. P. Bogert. 1950. A dynamical theory of the cochlea. *J. Acoust. Soc. Am.* 22:369–381.

27. Steele, C. R., and L. A. Taber. 1979. Comparison of WKB calculations and experimental results for three-dimensional cochlear models. *J. Acoust. Soc. Am.* 65:1007–1018.

28. Yoon, Y. J., S. Puria, and C. R. Steele. 2007. Intracochlear pressure and derived quantities from a three-dimensional model. *J. Acoust. Soc. Am.* 122:952–966.

29. de Boer, E. 1996. Mechanics of the cochlea: modeling efforts. The Cochlea. Springer, Berlin, Germany, pp. 258–317.

30. Olson, E. S. 1998. Observing middle and inner ear mechanics with novel intracochlear pressure sensors. *J. Acoust. Soc. Am.* 103:3445–3463.

31. Olson, E. S. 1999. Direct measurement of intra-cochlear pressure waves. *Nature.* 402:526–529.

32. Olson, E. S. 2001. Intracochlear pressure measurements related to cochlear tuning. *J. Acoust. Soc. Am.* 110:349–367.

33. Dong, W. 2017. Simultaneous intracochlear pressure measurements from two cochlear locations: propagation of distortion products in gerbil. *J. Assoc. Res. Otolaryngol.* 18:209–225.

34. Kale, S. S., and E. S. Olson. 2015. Intracochlear scala media pressure measurement: implications for models of cochlear mechanics. *Biophys. J.* 109:2678–2688.

35. Meaud, J., and K. Grosh. 2012. Response to a pure tone in a nonlinear mechanical-electrical-acoustical model of the cochlea. *Biophys. J.* 102:1237–1246.

36. Meaud, J., and K. Grosh. 2014. Effect of the attachment of the tectorial membrane on cochlear micromechanics and two-tone suppression. *Biophys. J.* 106:1398–1405.

37. Meaud, J., and C. Lemons. 2015. Nonlinear response to a click in a time-domain model of the mammalian ear. *J. Acoust. Soc. Am.* 138:193–207.

38. Ramamoorthy, S., N. V. Deo, and K. Grosh. 2007. A mechano-electro-acoustical model for the cochlea: response to acoustic stimuli. *J. Acoust. Soc. Am.* 121:2758–2773.

39. Meaud, J., and K. Grosh. 2010. The effect of tectorial membrane and basilar membrane longitudinal coupling in cochlear mechanics. *J. Acoust. Soc. Am.* 127:1411–1421.

40. Parthasarathi, A. A., K. Grosh, and A. L. Nuttall. 2000. Three-dimensional numerical modeling for global cochlear dynamics. *J. Acoust. Soc. Am.* 107:474–485.

41. Edge, R. M., B. N. Evans, …, P. Dallos. 1998. Morphology of the unfixed cochlea. *Hear. Res.* 124:1–16.

42. Richter, C.-P., G. Emadi, …, P. Dallos. 2007. Tectorial membrane stiffness gradients. *Biophys. J.* 93:2265–2276.

43. Ren, T., and A. L. Nuttall. 2001. Basilar membrane vibration in the basal turn of the sensitive gerbil cochlea. *Hear. Res.* 151:48–60.

44. Overstreet, E. H., 3rd, A. N. Temchin, and M. A. Ruggero. 2002. Basilar membrane vibrations near the round window of the gerbil cochlea. *J. Assoc. Res. Otolaryngol.* 3:351–361.

45. Dong, W., and E. S. Olson. 2013. Detection of cochlear amplification and its activation. *Biophys. J.* 105:1067–1078.

46. Dong, W., and E. S. Olson. 2006. Middle ear forward and reverse transmission in gerbil. *J. Neurophysiol.* 95:2951–2961.

47. Elliott, S. J., E. M. Ku, and B. Lineton. 2007. A state space model for cochlear mechanics. *J. Acoust. Soc. Am.* 122:2759–2771.

48. Kalluri, R., and C. A. Shera. 2001. Distortion-product source unmixing: a test of the two-mechanism model for DPOAE generation. *J. Acoust. Soc. Am.* 109:622–637.

49. Wang, Y., C. R. Steele, and S. Puria. 2016. Cochlear outer-hair-cell power generation and viscous fluid loss. *Sci. Rep.* 6:19475.

50. Lamb, J. S., and R. S. Chadwick. 2011. Dual traveling waves in an inner ear model with two degrees of freedom. *Phys. Rev. Lett.* 107:088101.

51. Cormack, J., Y. Liu, …, S. M. Gracewski. 2015. Two-compartment passive frequency domain cochlea model allowing independent fluid coupling to the tectorial and basilar membranes. *J. Acoust. Soc. Am.* 137:1117–1125.

52. Liu, Y., S. M. Gracewski, and J. H. Nam. 2015. Consequences of location-dependent organ of Corti micro-mechanics. *PLoS One.* 10:e0133284.

53. Fernández, C. 1952. Dimensions of the cochlea (guinea pig). *J. Acoust. Soc. Am.* 24:519–523.

54. Richter, C.-P., R. Edge, …, P. Dallos. 2000. Development of the gerbil inner ear observed in the hemicochlea. *J. Assoc. Res. Otolaryngol.* 1:195–210.

55. Ghaffari, R., A. J. Aranyosi, and D. M. Freeman. 2007. Longitudinally propagating traveling waves of the mammalian tectorial membrane. *Proc. Natl. Acad. Sci. USA.* 104:16510–16515.

56. Puria, S. 2003. Measurements of human middle ear forward and reverse acoustics: implications for otoacoustic emissions. *J. Acoust. Soc. Am.* 113:2773–2789.

57. Shera, C. A., and G. Zweig. 1991. Reflection of retrograde waves within the cochlea and at the stapes. *J. Acoust. Soc. Am.* 89:1290–1305.

58. de la Rochefoucauld, O., W. F. Decraemer, …, E. S. Olson. 2008. Simultaneous measurements of ossicular velocity and intracochlear pressure leading to the cochlear input impedance in gerbil. *J. Assoc. Res. Otolaryngol.* 9:161–177.

59. Overstreet, E. H., 3rd, and M. A. Ruggero. 2002. Development of wide-band middle ear transmission in the Mongolian gerbil. *J. Acoust. Soc. Am.* 111:261–270.

60. Johnson, S. L., M. Beurg, …, R. Fettiplace. 2011. Prestin-driven cochlear amplification is not limited by the outer hair cell membrane time constant. *Neuron.* 70:1143–1154.

61. Iwasa, K. H., and M. Adachi. 1997. Force generation in the outer hair cell of the cochlea. *Biophys. J.* 73:546–555.

62. Dallos, P., and B. N. Evans. 1995. High-frequency motility of outer hair cells and the cochlear amplifier. *Science.* 267:2006–2009.

63. Strelioff, D. 1973. A computer simulation of the generation and distribution of cochlear potentials. *J. Acoust. Soc. Am.* 54:620–629.

64. Greenwood, D. D. 1990. A cochlear frequency-position function for several species—29 years later. *J. Acoust. Soc. Am.* 87:2592–2605.

Supplemental Information

Forward and Reverse Waves: Modeling Distortion Products in the Intra-cochlear Fluid Pressure

Thomas Bowling and Julien Meaud

Forward and reverse waves: modeling distortion products in the intracochlear fluid pressure
T. Bowling and J. Meaud

A   Supplemental methods

A.1   Model Formulation

The mathematical model is formulated in the same manner as in our recent work [1], with the only difference being in how the middle ear is represented (here we only model the stapes, while a 2 degree-of-freedom model of the middle ear was used in Ref. [1]). As described in [2], the model includes degrees of the freedom for the acoustic fluid (the fluid pressure), the organ of Corti mechanics (at each section, it includes displacement degrees of the freedom for the BM and the TM) and electrical degrees of freedom (the electrical potential in the scala media, SV, ST and OHCs). Because the fluid is treated as inviscid and incompressible, the governing equation for the fluid is the Laplace equation ($\nabla^2 P = 0$); the governing equation for the organ of Corti is obtained from Lagrange's equations while the governing equations for the electrical degrees of freedom is obtained using Kirchoff's equation. The governing partial differential equations are transformed into the following system of ordinary differential equations using the finite element method:

$$
\begin{pmatrix} \mathbf{M_s} & \mathbf{0} & \mathbf{0} \\ \mathbf{M_{sf}} & \mathbf{0} & \mathbf{0} \\ \mathbf{0} & \mathbf{0} & \mathbf{0} \end{pmatrix} \begin{pmatrix} \ddot{\mathbf{u}} \\ \ddot{\mathbf{p}} \\ \ddot{\phi} \end{pmatrix} + \begin{pmatrix} \mathbf{C_s} & \mathbf{0} & \mathbf{0} \\ \mathbf{0} & \mathbf{0} & \mathbf{0} \\ \mathbf{C_{es}} & \mathbf{0} & \mathbf{C_e} \end{pmatrix} \begin{pmatrix} \dot{\mathbf{u}} \\ \dot{\mathbf{p}} \\ \dot{\phi} \end{pmatrix} + \begin{pmatrix} \mathbf{K_s} & \mathbf{K_{fs}} & \mathbf{K_{se}} \\ \mathbf{0} & \mathbf{K_f} & \mathbf{0} \\ \mathbf{K_{es}^{lin}} & \mathbf{0} & \mathbf{K_e} \end{pmatrix} \begin{pmatrix} \mathbf{u} \\ \mathbf{p} \\ \phi \end{pmatrix} + \begin{pmatrix} \mathbf{0} \\ \mathbf{0} \\ \mathbf{F_{es}^{NL}(u)} \end{pmatrix} = \begin{pmatrix} \mathbf{F_u} \\ \mathbf{0} \\ \mathbf{0} \end{pmatrix} \quad \text{(S1)}
$$

where $\mathbf{u}$ the vector of the structural displacements (with the displacement of the stapes as the first element), $\mathbf{p}$ is the vector of intracochlear fluid pressures, ϕ is the vector of electrical potentials, $\mathbf{F_{es}^{NL}}$ is a nonlinear term that arises due to nonlinearities in I_{MET} (see Refs. [3, 1] and Eq. 4 in the manuscript) , and $\mathbf{F_u} = [f(t), 0 \cdots 0]^T$ where $f(t)$ is the stimulus force applied on the stapes. The mechanical, acoustic, and electrical domains are coupled through the off-diagonal matrices on the left side of Eq. S1. In the linearized version of the model, $\mathbf{F_{es}^{NL}}$ is linearized while it is kept as a nonlinear term in the nonlinear version of the model. The process for formulating Eq. S1 in state space form is described in Ref. [1].

A.2   Model Parameters

Model parameters here have been adjusted from those of the guinea pig to represent the gerbil cochlea. Any model parameter not listed here is given in [2].

A.2.1   Geometrical parameters

The geometric parameters for the micromechanical model are shown in Table S1. A comparison of the anatomical model with images from Edge *et. al* [4] is shown in Figure S1.
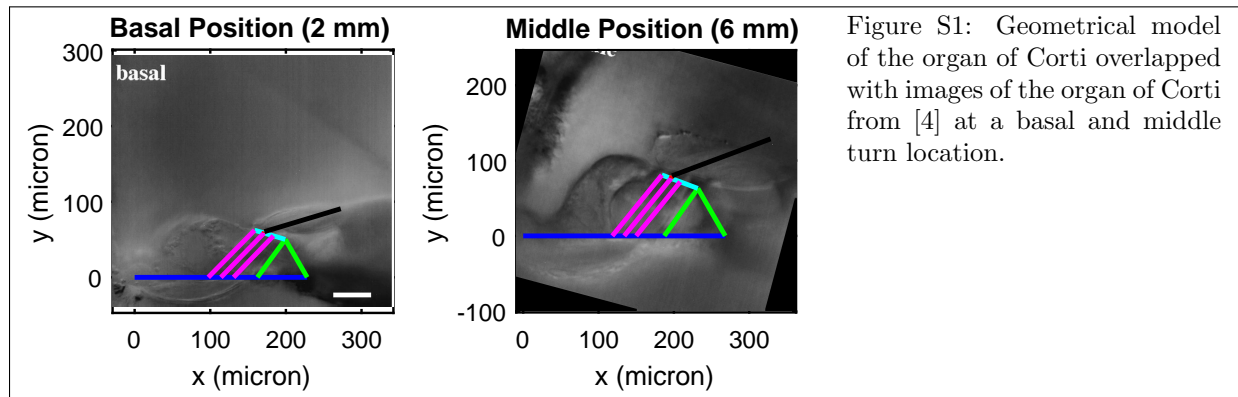

Figure S1: Geometrical model of the organ of Corti overlapped with images of the organ of Corti from [4] at a basal and middle turn location.

Table S1: Anatomical parameters for the model (x in cm).

Parameters	Description	Value
L	Length of BM	1.12 cm
L_h	Length of Helicotrema	0.1 cm
w	Width of cochlear ducts	0.1 cm
h	Height of each cochlear duct	0.1 cm
A_s	Cross-sectional area of stapes	$A_s = hw = 0.01$ cm^2
b	Width of BM	208μm (base) to 320μm (apex)
L_{tm}	Length of TM from pivot to middle HB	88μm (base) to 184μm (apex)
α	Angle between RL and BM	$15°$ (base) to $26°$ (apex)
β	Angle between HB and vertical	$15°$ (base) to $26°$ (apex)
L_0	Distance between left edge of BM and contact of middle OHC with BM	$b/2$
L_1	Radial distance between HBs	$13\ \mu$m
L_{pc}	Distance between left edge of BM and contact of outer pillar cell	58μm (base) to 100μm (apex)
L_{hb}	Length of HBs	1μm (base) to 6μm (apex)
L_{ro}	Distance between RL pivot and middle OHC	25.1μm (base) to 49μm (apex)
θ_1	Angle between inner pillar cell and BM	$60°$
θ_2	Angle between inner and outer pillar cells	$60°$

A.2.2 Mechanical parameters

Cochlear model

Table S2: Mechanical parameters for the cochlear model (x in cm). Parameters denoted * are defined per unit length.

Parameters	Description	Value	Ref.
K_{bm}	BM stiffness *	$18.4\exp(-7.54x) \times 10^5$ N/m^2	assumed
D_{xx}	BM plate bending stiffness (xx) *	$10^{-10}\exp(-0.5x)$ N.m	[5]
D_{xy}	BM plate bending stiffness (xy) *	$10^{-10}\exp(-0.5x)$ N.m	[5]
D_{shear}	BM plate bending stiffness (shear) *	$4.3\exp(-0.5x) \times 10^{-11}$ N.m	[5]
K_{tms}	TM shear stiffness *	$2.31\exp(-1.32x^2 - 6.42x) \times 10^5$ N/m^2	assumed
K_{tmb}	TM bending stiffness *	$3.84\exp(-7.54x) \times 10^4$ N/m^2	assumed
K_{rl}	RL stiffness *	$2.78\exp(-7.54x) \times 10^3$ N/m^2	assumed
K_{ohc}	OHC stiffness *	$5.07\exp(-7.54x) \times 10^3$ N/m^2	assumed
K_{hb}	HB stiffness *	$291\exp(-7.54x)$ mN/m	assumed
M_{bm}	BM mass *	2.8×10^{-7} kg/m	[6]
M_{tms}	TM shear mass *	$3.58\exp(1.58x) \times 10^{-6}$ kg/m	based on [7, 8]
M_{tmb}	TM bending mass *	$1.12\exp(2.15x) \times 10^{-6}$ kg/m	based on [7, 8]
c_{bm}	BM damping coefficient *	8.5×10^{-2} N.s/m^2	assumed
c_{hb}	HB damping coefficient	$\eta_f \frac{L_{tm}}{3L_{hb}}$, where $\eta_f = 1.0 \times 10^{-3}$ N.s/m^2 is the viscosity of the fluid	[5]
c_{tmb}	TM bending damping coefficient *	0.1 N.s/m^2	assumed
c_{tms}	TM shearing damping coefficient *	3×10^{-3} N.s/m^2	assumed
G_{tms}	TM shear modulus	$7.0\exp(-3.75x)$ kPa	[8, 5]
η_{tms}	TM shear viscosity	0.03 Pa.s	[9], based on [10]
ρ_f	fluid density	1000 kg/m^3	

Middle ear model

When reverse fluid waves reach the stapes, some of the wave energy is transmitted through the middle ear

and out into the ear canal while the rest is reflected back towards the apex as a forward traveling wave. In the frequency domain, the reverse middle ear impedance (*i.e*, the impedance looking out from the stapes in the reverse direction [11]) is given by:

$$Z_{meR} = \frac{1}{A_s^2}\left[M_s i\omega + C_s + \frac{K_s}{i\omega}\right] \tag{S2}$$

where M_s, C_s and K_s are the mass, damping coefficient, and stiffness coefficient of the stapes, respectively; ω is the radian frequency and A_s is the area of the stapes footplate. The stapes reflection coefficient is given as [12]:

$$R_{st} = \frac{Z_{meR}/Z_c^* - 1}{Z_{meR}/Z_c + 1} \tag{S3}$$

where R_{st} is the stapes reflection coefficient, Z_c is the input impedance of the cochlear model, and $*$ denotes the complex conjugate. The values of the stapes reflection coefficient, R_{st}, cochlear input impedance, Z_c, and reverse middle ear impedance, Z_{meR}, are presented in Fig. S2 Because there are no measurements of the middle ear reverse impedance or stapes reflection coefficient in the gerbil ear, the value of the middle ear parameters were chosen such that the reflection coefficient is similar to what has been reported in the human [11]. The mechanical parameters for the middle ear model are presented in Table S3. All results in the manuscript are obtained with the baseline model. In addition to the baseline model, models with small and large stapes reflection coefficient magnitudes, $|R_{st}|$, where developed. The effects of varying the magnitude of R_{st} on DP propagation are shown in Fig. S9.

Table S3: Mechanical parameters for the middle ear model.

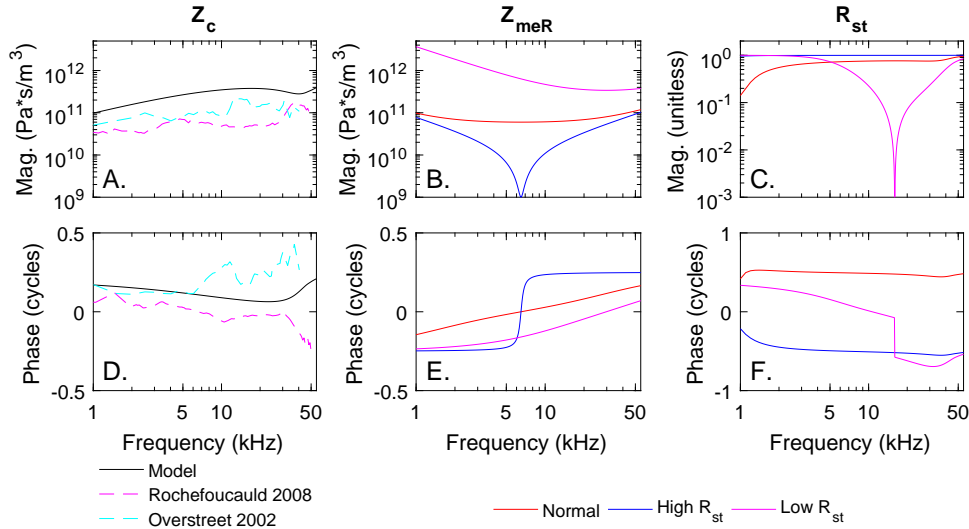| Parameters	Description	Baseline	High $|R_{st}|$	Low $|R_{st}|$
M_s	Stapes mass (kg)	3.0×10^{-7}	3.0×10^{-7}	6.6×10^{-7}
C_s	Stapes damping coefficient (N.s/m)	6.0×10^{-2}	1.0×10^{-3}	3.4×10^{-1}
K_s	Stapes stiffness (N/m)	5.0×10^{2}	5.0×10^{2}	2.3×10^{4}

Figure S2: Different middle ear models. A. and D. Magnitude and phase of the cochlear input impedance, compared to data from [13, 14]. The model cochlear input impedance is computed by taking the ratio of the scala vestibuli pressure next to the stapes to the volume velocity of the stapes. B.,E. Magnitude and phase of the reverse impedance of the middle ear model. C.,F. Magnitude and phase of the stapes reflection coefficient.

A.2.3 Electrical parameters

The electrical parameters for the cochlear model are shown in Table S4. The value of the basolateral conductance and capacitance were set to the values reported in [15]. The HB saturating conductance, G_a^{max}, was chosen to be a free parameter whose value was varied during the calibration process to give BM gain values that matches the experimental data from [16, 17]. The value of the conductance is somewhat higher than the values reported by Johnson et al. [15] in the gerbil cochlea. As in [3], the constants ΔX and X_0 of Eq. 4 are given by

$$\Delta X = \frac{f_{gs}\gamma}{k_B T} \tag{S4}$$

$$X_0 = \Delta X \log(1/P_0^s - 1) \tag{S5}$$

where $f_{gs} = 10$ pN is the single channel gating force in the tip link direction, $\gamma = 0.5\mu m/L_{hb}$ is the geometrical gain factor, k_B is the Boltzmann constant, $T = 37°C$ is the temperature, and P_0^s is the resting probability of the MET channel (assumed to be equal to 0.4).

Table S4: Electrical parameters for the model (x in cm).

Parameters	Description	Value	Ref.
C_m	Basolateral capacitance	$52.35x$ pF	based on [15]
G_m	Basolateral conductance	$64 - 49.6x$ nS	based on [15]
ϵ_3	Electromechanical coupling coefficient	$1.04 + 0.36x$ N/m/mV	based on [18]
$1/R_a^0$	apical resistance	$172\exp(-2.05x)$ nS	[3]
G_a^{max}	saturating HB conductance	Interpolated from 479 nS at x=0cm 427 nS at x=0.15cm 324 nS at x=0.224 cm 151 nS at x=0.44 cm 60 nS at x=0.67 cm 14.8 nS at x=1.12 cm	assumed
C_a	apical capacitance	50 nF/m	based on [19]
R_{tl}	resistance from ST to ground	4 Ωm	based on [20]
R_{vm}	resistance from SV to SM	25 Ωm	based on [20]
R_{vl}	resistance from SV to ground	10 Ωm	based on [20]
P_0^s	resting probability	0.4	[3]
ΔV_{hb}^0	resting value of potential difference between scala media and intracellular OHC potential	$150 - 10x$ mV	[3]

A.3   Decomposition into forward and reverse wave components

To make sure that the two forward and reverse wave components, $P_{as}^{DP,f}$ and $P_{as}^{DP,r}$, satisfy the boundary condition at the stapes, we used the following approach. At the base, the pressure is approximately 1D such that it only depends on x; the y and z dependence of the pressure can be omitted. Eq. 11 does not specify the values of the Fourier transform of $P_{as}^{DP,f}$ and $P_{as}^{DP,r}$ at $k = 0$. To find these values, the value of $\tilde{P}_{as}^{DP,f}(k = 0)$ and $\tilde{P}_{as}^{DP,r}(k = 0)$ are assumed to be given by:

$$\tilde{P}_{as}^{DP,f}(k = 0) = \alpha_P \tilde{P}_{as}^{DP}(k = 0) \tag{S6}$$

$$\tilde{P}_{as}^{DP,r}(k = 0) = (1 - \alpha_P)\tilde{P}_{as}^{DP}(k = 0) \tag{S7}$$

where α_P is a complex number. At the stapes, the forward and reverse waves should satisfy:

$$R_{st} = \frac{P_{as}^{DP,f}(x = 0)}{P_{as}^{DP,r}(x = 0)} \tag{S8}$$

Using the definition for the discrete Fourier transform:

$$\begin{aligned}
P_{as}^{DP,f}(x = 0) &= \frac{1}{N}\sum_{I=1}^{N}\tilde{P}_{as}^{DP,f}(k_I) \\
&= \frac{1}{N}\left[\alpha\tilde{P}_{as}^{DP}(k = 0) + \sum_{k>0}\tilde{P}_{as}^{DP,f}(k)\right]
\end{aligned} \tag{S9}$$

and

$$\begin{aligned}
P_{as}^{DP,r}(x = 0) &= \frac{1}{N}\sum_{I=1}^{N}\tilde{P}_{as}^{DP,r}(k_I) \\
&= \frac{1}{N}\left[(1 - \alpha_P)\tilde{P}_{as}^{DP}(k = 0) + \sum_{k<0}\tilde{P}_{as}^{DP,r}(k)\right],
\end{aligned} \tag{S10}$$

where N is the number of samples. Eq. S8 is solved for α_P to yield:

$$\alpha_P = \frac{\left[\tilde{P}_{as}^{DP}(k = 0) + \sum\limits_{k<0}\tilde{P}_{as}^{DP}(k)\right]R_{st} - \sum\limits_{k>0}\tilde{P}_{as}^{DP}(k)}{(1 + R_{st})\tilde{P}_{as}^{DP}(k = 0)}. \tag{S11}$$

From here, all parameters are known and the forward and reverse waves are calculated using Eqs. 9 and 10. This same procedure can be applied to the BM velocity to find its forward and reverse wave components. The BM velocity is decomposed into forward and reverse component, $v_{bm}^{DP,f}$ and $v_{bm}^{DP,r}$. The value of $\tilde{v}_{bm}^{DP,f}(k = 0)$ and $\tilde{v}_{bm}^{DP,r}(k = 0)$ are assumed to be given by:

$$\tilde{v}_{bm}^{DP,f}(k = 0) = \alpha_{bm}\tilde{v}_{bm}^{DP}(k = 0) \tag{S12}$$

$$\tilde{v}_{bm}^{DP,r}(k = 0) = (1 - \alpha_{bm})\tilde{v}_{bm}^{DP}(k = 0) \tag{S13}$$

where α_{bm} is a complex number. Satisfaction of the boundary conditions at x=0 requires that:

$$\alpha_{bm} = \frac{R_{st}\left[\tilde{v}_{bm}^{DP}(k = 0) + \sum\limits_{k<0}\tilde{v}_{bm}^{DP}(k)\right] - \sum\limits_{k>0}\tilde{v}_{bm}^{DP}(k)}{(1 + R_{st})\tilde{v}_{bm}^{DP}(k = 0)}. \tag{S14}$$

B   Supplemental results

B.1   Fluid Mode Convergence

A convergence study was performed to determine the number of fluid modes needed to accurately capture the 3D nature of the fluid. The effect of the number of modes included on the pressure magnitude at the 20 kHz BP is shown in Fig. S3. For this convergence study, the results for the model with 75 fluid modes was used as the reference. In Fig. S3A, while there is significant variation in the magnitude for 1, 3, and 8 modes at $y = 0$, for 25 modes the results matches very closely with the results for 75 modes. The relative percent error of the fluid pressure shown in Fig. S3B is given by:

$$E_i = \left| \frac{P_{T,75} - P_{T,i}}{P_{T,75}} \right| \times 100\% \tag{S15}$$

where $P_{T,75}$ is the complex value of the pressure at $y = 0$ for the model with 75 fluid modes, and $P_{T,i}$ is the complex value of the pressure for the model with i fluid modes. While the magnitude difference is fairly large for a model with only 1 mode, by 9 modes the pressure magnitude is within 0.1 dB of the 75 mode pressure magnitude and relative error of 1.2 percent. Although fewer modes (but more than 9) could have been used to accurately model the pressure, in this work 25 modes were used. There is a fairly significant increase in computational cost when using more fluid modes during matrix assembly; however the finite element matrices were assembled once and then loaded from a file for each simulation. Once the matrices are assembled, the number of modes has no influence on the computational time needed to solve Eq. S1 using the state-space approach we previously described in [1].
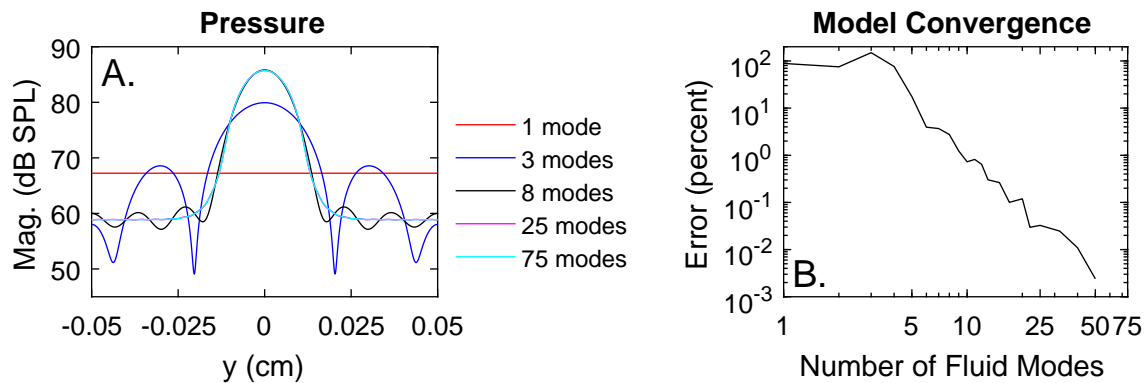

Figure S3: Convergence study for the number of fluid modes at z=0 in the SV at 20 kHz and its BP. A. Radial variations of the pressure magnitude. B. Relative percent error of the fluid pressure at y=0 relative to model with 75 pressure modes.

B.2 Comparison of model simulation for the pure tone pressure to experiments

The pure tone pressure response of the model is compared with experimental pressure measurements in two different animals [21] in Fig. S4. In Fig. S4A for the pressure 15 μm away from the BM, the model peaks in magnitude 2 dB higher than the experimental results, while in Fig. S4B, the model pressure peaks in magnitude nearly 16 dB lower than the experimental results for a 60 dB SPL stimulus. Given the variability in the experimental magnitudes, the model results for the peak magnitude are realistic. In Fig. S4, a high frequency plateau is observed in the magnitude, both for the model and the experiments; this plateau corresponds to the symmetric pressure components. The notches for the model results at 115 μm in Fig. S4A are due to interactions between the symmetric and antisymmetric pressure components. As with the BM velocity results, the model pressure phase decreases at a faster rate than the experimental results.
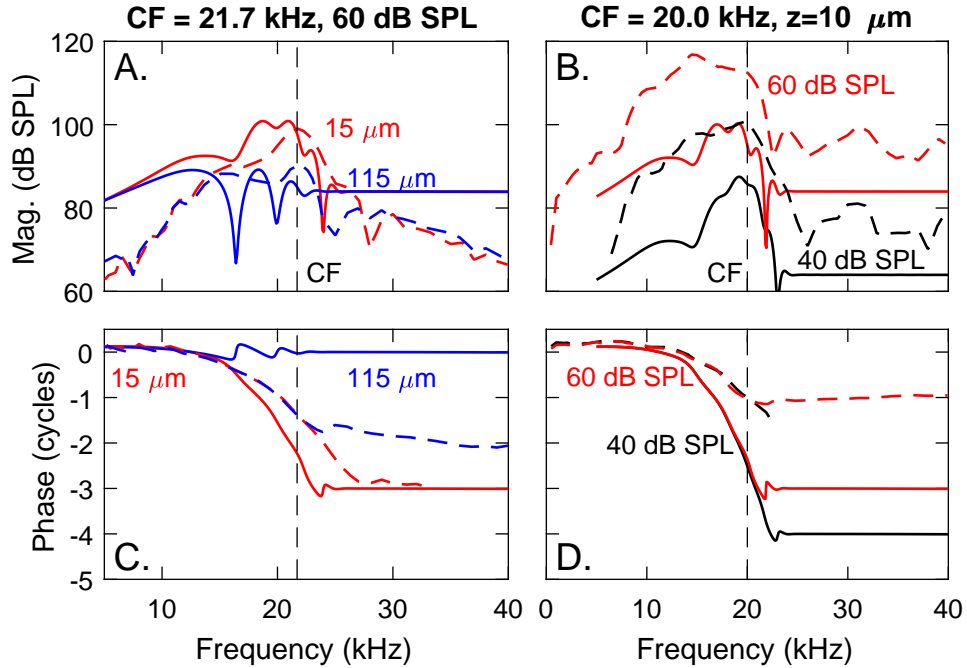

Figure S4: Comparison of fluid pressure pure tone responses for model and experimental data from [21] for 40 and 60 dB SPL stimuli. Experimental results in (A,C) and (B,D) were taken from Figs. 4 and 6, respectively, of [21]. (A-B) Magnitude. (C-D) Phase. All model phases and the experimental phases in D. are taken relative to the pressure at the stapes, while the experimental phases in C. are taken relative to the ear canal pressure. Pressures were taken at 15 and 115 μm from the BM in the ST for a 60 dB SPL stimuli (A,C) and 10 μm from the BM in the ST for 40 and 60 dB SPL stimuli (B,D). Model results are drawn with solid lines and experimental results with dashed lines.

B.3 Pure tone response at all longitudinal positions

The response of the model at all longitudinal locations is now considered with the place-frequency map, gain at CF, and quality factor shown in Fig. S5. The results in the section were obtained using a linear formulation of the model. The active model represents the response at a low stimulus level while the passive model is analogous to the response at a high stimulus level (because the feedback from outer hair cells saturates such that it has almost no effect on the acoustic response of the system at a high sound pressure level). The passive model is obtained by setting $G_{hb}^{max} = 0$ (and thus $I_{MET} = 0$). In Fig. S5A, the passive and active model place-frequency maps are compared with experimental data from [16, 17] and Greenwood's place-frequency map [22] for the gerbil cochlea. In this work, we consider the characteristic frequency (CF) to be the frequency of peak magnitude for the active linear model for a given position, which is given by the active place-frequency map. The passive model place-frequency map is in good agreement with Greenwood's map at all positions. At more basal positions, the relative frequency spacing between passive and active models for a given position matches the experimental results from [17]. At the more apical position, the frequency difference between passive and active models for a given position is larger than that of the experimental results from [16]. The gain of the BM relative to the passive model is calculated as

$$G_{bm}^{active/passive}(x) = \frac{\max_{\omega} |G_{bm}^{active}(x, \omega)|}{\max_{\omega} |G_{bm}^{passive}(x, \omega)|} \tag{S16}$$

where G_{bm}^{active} is the gain of the BM velocity relative to the stapes for the active model, $G_{bm}^{passive}$ is the gain of the BM velocity relative to the stapes for the passive model, and the maximum amplitude is taken across frequency for a given position. In Fig. S5B, the BM gain is plotted as a function of the CF of each location and is compared with the gain calculated from the measurements from [16, 17]. Across the range of frequencies of interest for this work, the model has at least 20 dB of gain from 7 to 40 kHz. Effort was made during the calibration process to match the experimental gain from [16, 17]. The tuning sharpness of the active model, evaluated using the quality factor, Q_{10dB}, is shown in Figure S5C. As shown in Figs. 3A and 3B, the model matches the tuning sharpness around 13 and 34 kHz best places from [16, 17]. The model has fairly broad tuning across frequency and becomes more broadly tuned towards the apex.
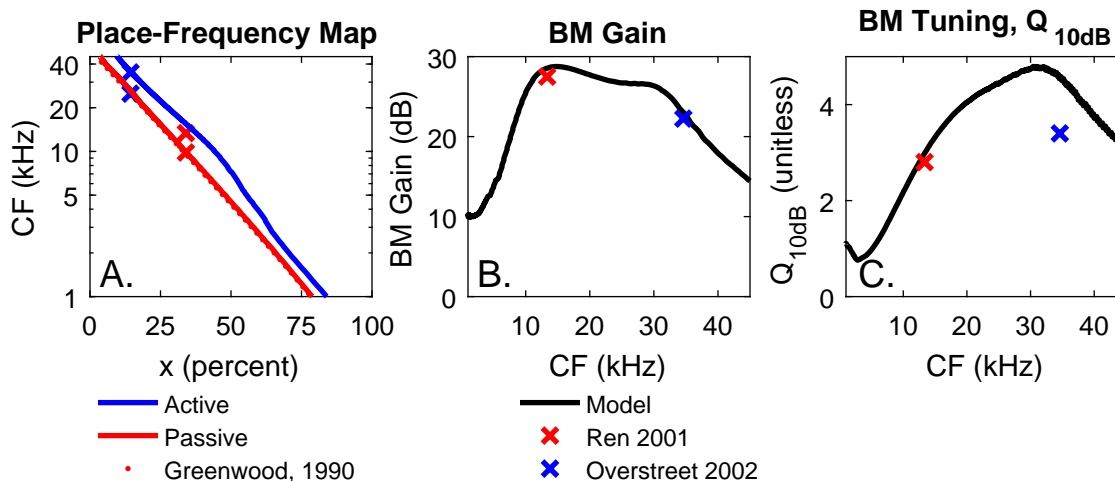

Figure S5: Comparison of BM pure tone response for model and experimental data from [22, 17, 16]. A. Place-frequency map of the passive and active models with data from [22, 17, 16]. B. Amplification of active model relative to passive model. C. Quality factor, Q_{10dB}, of the tuning of the BM. Model results are compared with measurements from the 13 kHz [16] and 34 kHz [17] best places.

B.4 Variations on Pressure with Distance from the BM

The spatial variations of the fluid pressure of the primary tones and DP obtained with the model are compared with pressure measurements by Dong and Olson [24] in Fig. S6. For these measurements, the primary frequencies were varied so that f_2, f_1, and f_{DP} were alternatively set to CF = 21 kHz. In all three cases, both model and experimental primaries show very little spatial variation. The DP decreases at a fast rate as the distance from the BM increases, both in the model simulations and the experiments; however, the slope seen in the model simulations is steeper than in the measurements. When the DPs from Fig. S6A-C are compared to a low intensity pure tone of the same frequency (Figs. S6D-F), similar decreases in magnitude with distance from the BM are found, which has also been observed experimentally (see Fig. 4B in [21]). However, the pure tone pressure converges to a higher value than the DP pressure at large distances from the BM because the pure tone symmetric pressure is higher than the DP symmetric pressure (Figs. S6G-I). The pure tone and DP antisymmetric pressure decrease at nearly the same rate and converge to approximately the same value. For all three cases, the antisymmetric pressure is much higher than the symmetric pressure close to the BM and decreases exponentially with increasing distance from the BM. Close to the BM, the antisymmetric pressure dominates the symmetric pressure, while farther from the BM the symmetric pressure dominates the antisymmetric pressure, at which point the total pressure varies little with distance from the BM.
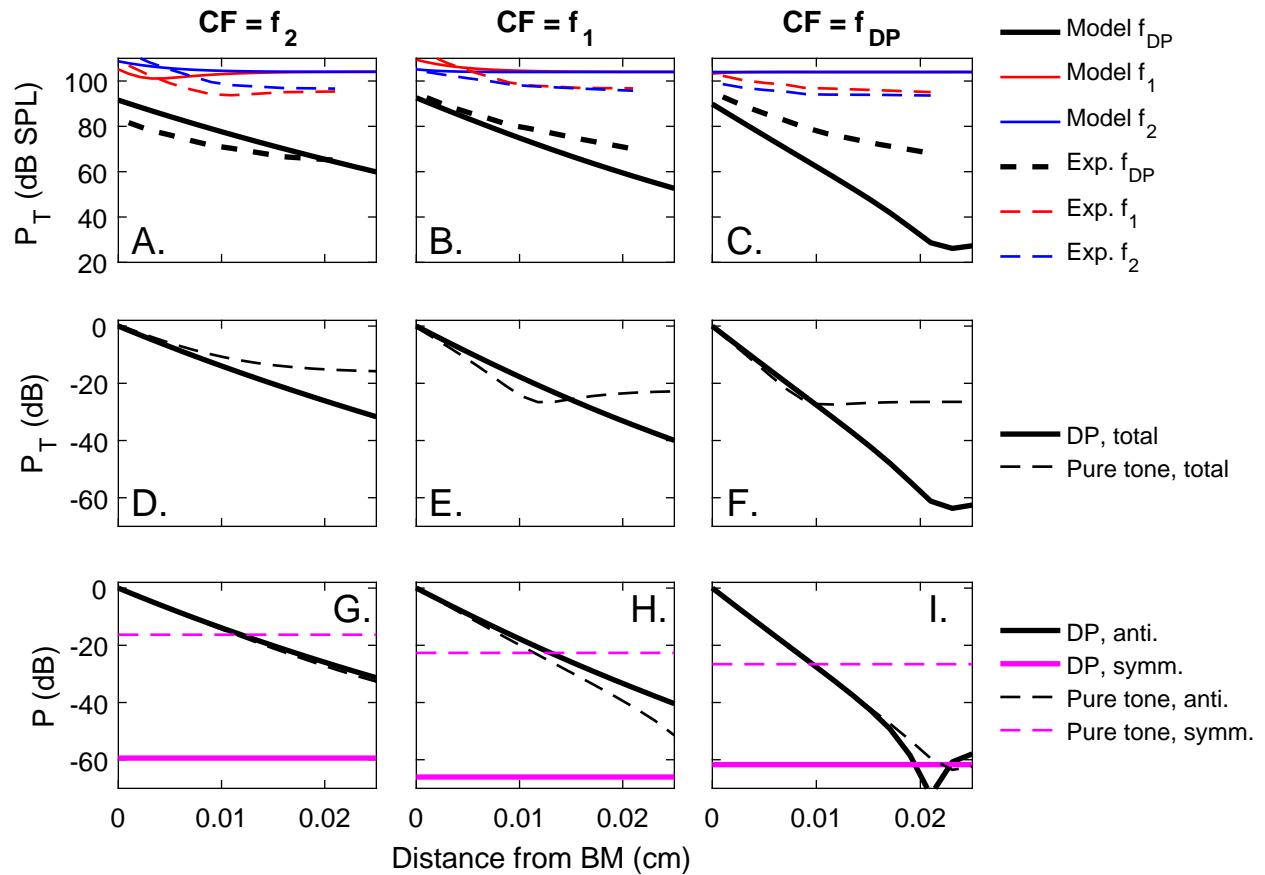

Figure S6: A-C. Comparison of pressure magnitude vs distance from BM in ST with data from [24]. D-F. Comparison of total pressure magnitude vs distance from BM in ST for DP and pure tone of the same frequency. G-I. Decomposition of the pressure from D-F into symmetric and antisymmetric components. Horizontal lines in G-I are the symmetric pressures. All model and experimental data were taken at the 21 kHz best place with primary stimuli of 80 dB SPL and f_2/f_1=1.10. The pure tone model results in D-I were obtained from the nonlinear model with a stimulus at 30 dB SPL. Magnitudes in D-I were normalized by the magnitude of the antisymmetric pressure at the BM, $P_{as}(z=0)$.

B.5 Effect of Varying Primary Stimulus Level

Nonlinear two-tone simulations for different primary stimuli levels are compared with experimental measurements taken by [21]. For both the 50 dB SPL model and experimental results the magnitude peaks near f_{DP}=CF, while for 80 dB SPL the model peaks near f_{DP}=CF and the experimental results peak at a slightly lower frequency (f_2=27 kHz). Both 50 and 80 dB SPL model results show a notch in magnitude and corresponding phase shift below 20 kHz; the notch and phase shift are due to the interference between the forward and reverse waves. Below this phase shift, the phase is either nearly flat or has a slight positive slope indicating a reverse wave.
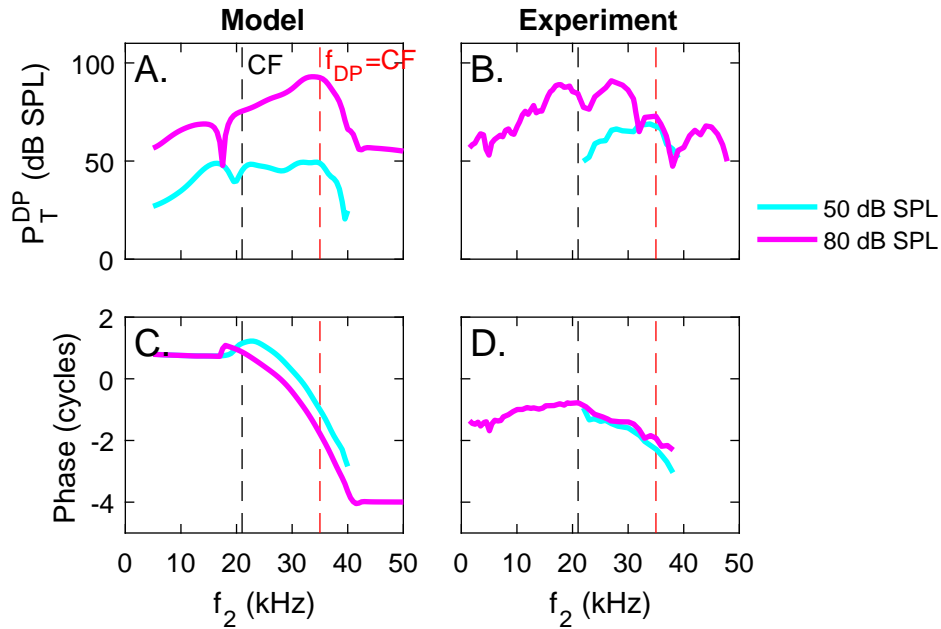

Figure S7: DP model and experimental measurements from [21] of fluid pressure for varied stimulus levels. Model results and experimental measurements were taken at 21 kHz BP in ST 10 μm from BM for f_2/f_1=1.25. The model phase is referenced to the pressure in the SV at the stapes and the experimental phase is taken relative to the ear canal pressure. A.,B. Magnitude of fluid pressure. C.,D. phase of fluid pressure.

B.6 Effect of Primary Frequency Ratio on Forward and Reverse Waves

The effect of varying the primary frequency ratio on the forward and reverse waves is shown in Fig. S8.
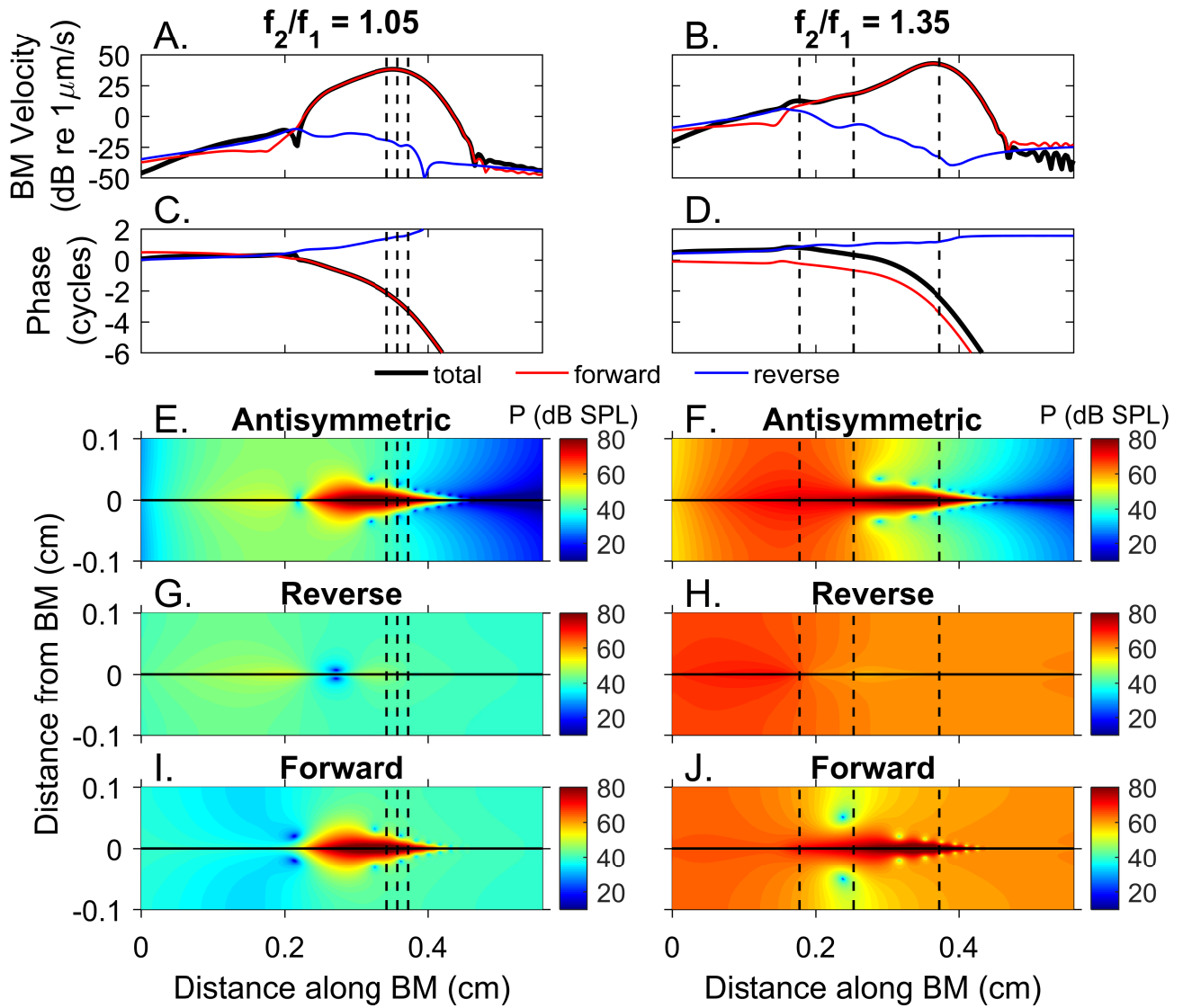

Figure S8: Decomposition of BM velocity and antisymmetric pressure at f_{DP} into forward and reverse waves for equi-level primaries of 80 dB SPL for $f_2/f_1 = 1.05$ and 1.35, and f_{DP}=16 kHz. A.,B. Magnitude of BM velocity. C.,D. Phase of BM velocity. E.,F. Magnitude of antisymmetric pressure. G.,H. Magnitude of reverse wave component of antisymmetric pressure. I.,J. Magnitude of forward wave component of antisymmetric pressure. The vertical dashed lines indicate, from left to right, the f_2, f_1, and f_{DP} best places.

B.7 Effect of Stapes Reflection on Forward and Reverse Waves

To investigate the role of the middle ear on DP propagation, two additional middle ear models were developed (see Table S3 and Fig. S2) (1) with a stapes reflection coefficient, R_{st}, of high magnitude across frequency and (2) with a stapes reflection coefficient of small magnitude at 16 kHz. The high $|R_{st}|$ is the case when most energy propagating in the reverse direction is reflected back into the cochlea, while for the low $|R_{st}|$ case very little of the reverse wave for f_{DP} is reflected back into the cochlea.

 The effect of varying the stapes reflection coefficient is investigated in Fig. S9. The most predominant changes in varying the stapes occur in the most basal regions, while closer to the DP best place the effect of the stapes variations appears negligible. For the high $|R_{st}|$ model, the forward and reverse waves have approximately the same magnitude while the phase differs by half a cycle (due to the phase of R_{st}). As a result of this phase difference, the total BM velocity and antisymmetric pressure close to the stapes is relatively small. For the low $|R_{st}|$ case, very little of the reverse wave is reflected at the stapes and thus the forward wave is very small at the stapes.
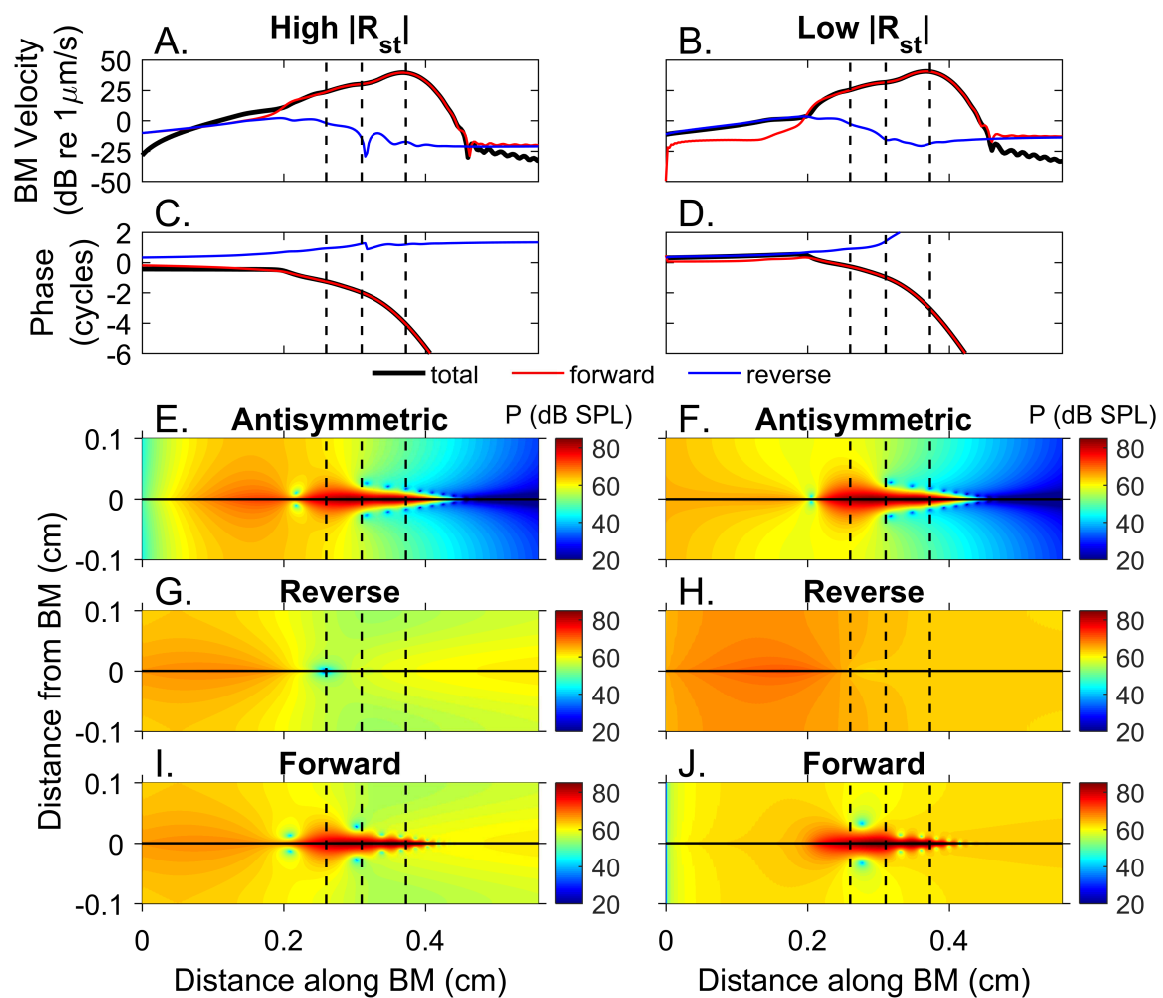

Figure S9: Decomposition of BM velocity and antisymmetric pressure at f_{DP} into forward and reverse waves for equi-level primaries of 80 dB SPL with $f_2/f_1 = 1.20$ and $f_{DP}=16$ kHz for different middle ear models. A.,B. Magnitude of BM velocity. C.,D. Phase of BM velocity. E.,F. Magnitude of antisymmetric pressure. G.,H. Magnitude of reverse wave component of antisymmetric pressure. I.,J. Magnitude of forward wave component of antisymmetric pressure. The vertical dashed lines indicate, from left to right, the f_2, f_1, and f_{DP} best places.

B.8   Movies

Movie S1. Movie of the steady state DP fluid pressure for equi-level primaries of 80 dB SPL with f_2/f_1=1.20 and $f_2 = 24$ kHz with the baseline middle ear model. All pressure components are normalized by the maximum total pressure value. Because most of the pressure amplitudes are much smaller than the maximum normalized pressure of 1, the colorbar limits were set to a smaller value (-0.05 to 0.05) to highlight the spatial variations of the pressure. The waveform shows the normalized total pressure at the stapes in the center of the SV.

Movie S2. Movie of the steady state DP fluid pressure for equi-level primaries of 80 dB SPL with f_2/f_1=1.20 and $f_2 = 24$ kHz with the Low $|R_{st}|$ middle ear model. All pressure components are normalized by the maximum total pressure value. Because most of the pressure amplitudes are much smaller than the maximum normalized pressure of 1, the colorbar limits of the pressure were set to a smaller value (-0.05 to 0.05) to highlight the spatial variations of the pressure. The waveform shows the normalized total pressure at the stapes in the center of the SV.

Supporting References

[1] Meaud, J. and C. Lemons. 2015. Nonlinear response to a click in a time-domain model of the mammalian ear. *J. Acoust. Soc. Am.* 138:193–207.

[2] Ramamoorthy, S., N. V. Deo, and K. Grosh. 2007. A mechano-electro-acoustical model for the cochlea: response to acoustic stimuli. *J. Acoust. Soc. Am.* 121:2758–2773.

[3] Meaud, J. and K. Grosh. 2012. Response to a pure tone in a nonlinear mechanical-electrical-acoustical model of the cochlea. *Biophys. J.* 102:1237–1246.

[4] Edge, R. M., B. N. Evans, M. Pearce, C.-P Richter, X. Hu, and P. Dallos. 1998. Morphology of the unfixed cochlea. *Hear. Res.* 124:1–16.

[5] Meaud, J. and K. Grosh. 2010. The effect of tectorial membrane and basilar membrane longitudinal coupling in cochlear mechanics. *J. Acoust. Soc. Am.* 127:1411–1421.

[6] Fernández, C. 1952. Dimensions of the cochlea (guinea pig). *J. Acoust. Soc. Am.* 24:519–523.

[7] Richter, C.-P., R. Edge, D. Z. Z. He, and P. Dallow. 2000. Development of the gerbil inner ear observed in the hemicochlea. *J. Assoc. Res. Otolaryngol.* 1:195–210.

[8] Richter, C.-P., G. Emadi, G. Getnick, A. Quesnel, and P. Dallos. 2007. Tectorial membrane stiffness gradients. *Biophys. J.* 93:2265–2276.

[9] Meaud, J., and K. Grosh. 2014. Effect of the attachment of the tectorial membrane on cochlear micromechanics and two-tone suppression. *Biophys. J.* 106:1398–1405.

[10] Ghaffari, R., A. J. Aranyosi, and D. M. Freeman. 2007. Longitudinally propagating traveling waves of the mammalian tectorial membrane. *Proc. Natl. Acad. Sci. U.S.A.* 104:16510–16515.

[11] Puria, S. 2003. Measurements of human middle ear forward and reverse acoustics: implications for otoacoustic emissions. *J. Acoust. Soc. Am.* 113:2773–2789.

[12] Shera, C. A. and G. Zweig. 1991. Reflection of retrograde waves within the cochlea and at the stapes. *J. Acoust. Soc. Am.* 89:1290–1305.

[13] de La Rochefoucauld, O., W. F. Decraemer, S. M. Khanna, and E. S. Olson. 2008. Simultaneous measurements of ossicular velocity and intracochlear pressure leading to the cochlear input impedance in gerbil. *J. Assoc. Res. Otolaryngol.* 9:161–177.

[14] Overstreet III, E. H. and M. A. Ruggero. 2002. Development of wide-band middle ear transmission in the Mongolian gerbil. *J. Acoust. Soc. Am.* 111:261–270.

[15] Johnson, S. L., M. Beurg, W. Marcotti, and R. Fettiplace. 2011. Prestin-driven cochlear amplification is not limited by the outer hair cell membrane time constant. *Neuron.* 70:1143–1154.

[16] T. Ren and A. L. Nuttall. 2001. Basilar membrane vibration in the basal turn of the sensitive gerbil cochlea. *Hear. Res.* 151:48–60.

[17] Overstreet III, E. H., A. N. Temchin, and M. A. Ruggero. 2002. Basilar membrane vibrations near the round window of the gerbil cochlea. *J. Assoc. Res. Otolaryngol.* 3:351–361.

[18] Iwasa, K. H. and M. Adachi. 1997. Force generation in the outer hair cell of the cochlea. *Biophys. J.* 73:546–555.

[19] Dallos, P. and B. N. Evans. 1995. High-frequency motility of outer hair cells and the cochlear amplifier. *Science.* 267:2006.

[20] Strelioff, D. 1973. A computer simulation of the generation and distribution of cochlear potentials. *J. Acoust. Soc. Am.* 54:620–629.

[21] Dong, W. 2017. Simultaneous intracochlear pressure measurements from two cochlear locations: Propagation of distortion products in gerbil. *J. Assoc. Res. Otolaryngol.* 18:209–225.

[22] Greenwood, D. D. 1990. A cochlear frequency-position function for several species? 29 years later. *J. Acoust. Soc. Am.* 87:2592–2605.

[23] Dong, W. and E. S. Olson. 2013. Detection of cochlear amplification and its activation. *Biophys. J.* 105:1067–1078.

[24] Dong, W. and E. S. Olson. 2005. Two-tone distortion in intracochlear pressure. *J. Acoust. Soc. Am.* 117:2999–3015.